Karlsruhe Institute of Technology

Energy calibration of the scintillation detectors of the IceCube Surface Array Enhancement

Energiekalibrierung der Szintillatordetektoren des IceCube Surface Array Enhancement

Bachelor's Thesis of

Laura Lehmann

at the KIT Faculty of Physics
Institute for Astroparticle Physics (IAP)
Institute of Experimental Particle Physics (ETP)

Reviewer:	Prof. Dr. R. Engel
Second reviewer:	Dr. A. Haungs
Advisor:	M. Sc. Shefali

05. December 2022 – 23. June 2023

Abstract

Energy calibration of the scintillation detectors of the IceCube Surface Array Enhancement

The Surface Array Enhancement is a planned extension of the IceCube Neutrino Observatory located at the geographic South Pole. It supports IceTop, which is namely the surface array of the neutrino detector. IceTop serves as veto for the events measured in the in-ice array, but is furthermore an independent cosmic-ray detector. The measurements of IceTop are influenced by systematic uncertainties, such as signal attenuation due to snow accumulations. Therefore, the Surface Array Enhancement consisting of scintillation detectors as well as radio antennas is foreseen. This addition is not only planned to minimize the uncertainties, but also to increase the sky coverage and enhance the progress towards current research objectives. The hybrid detector field is planned to be installed over the footprint of the IceCube array comprising 32 stations, each consisting of eight scintillation detectors and three radio antennas.
This thesis focuses on the scintillation detectors and performs an energy calibration. The main objective is to find a relation between the digitized light signal (ADC-channel) from the scintillators and the corresponding deposited energy due to the particle interaction. This represents an important part of the entire calibration chain for the scintillators in the air-shower measurements and their interpretation. In this thesis it is achieved by the utilization of various radioactive sources, each with an energy spectrum lower than the range of the particle peak. The energy spectrum of the active sources is well studied and known, whereas the relation between the measured ADC-channel and the energy deposit of muons, for example, contains still relevant uncertainties. The active source is placed in varying positions near the panel and measured in several measurement series. Overall three distinct sources were used: Na22, Cs137 and Co60. The positioning, duration and outside preconditions vary over the measurement series to find the most validate experimental requirements.
While performing a measurement with a source nearby the scintillation detectors, the Compton edges of the energy deposit from the sources are represented in the charge spectrum. The resembling energy deposit is interpreted as 70% of the peaks mean count-rate, which is estimated by a Gaussian fit. This leads to a valid assignment between the digitized signal and the particular energy deposit. Furthermore, a linear coherence was ascertained and the ADC-value for the simple particle peak assigned. The linear relation of ADC-value and deposited energy could be confirmed.

Zusammenfassung

Energiekalibrierung der Szintillatordetektoren des IceCube Surface Array Enhancement

Das Surface Array Enhancement ist eine Erweiterung des IceCube Neutrino Observatoriums am geographischen Südpol. Es dient zur Verbesserung der Funktionalität von IceTop, dem Oberflächen-Messfeld von IceCube. IceTop fungiert sowohl als Veto für gemessene Ereignisse des In-Eis-Detektors, als auch als eigenständiger Detektor für die Messung ausgedehnter Luftschauer der kosmischen Strahlung. Allerdings sind diese Messungen mit sytematischen Unsicherheiten behaftet, wie beispielsweise bedingt durch die Schwankungen der Schneehöhe auf den Detektoren. Daher ist das Surface Array Enhancement vorgesehen, welches eine Erweiterung des Oberflächen-Detektorfelds durch mehrere Szintillatordetektoren und Radioantennen darstellt. Das zusätzliche Messfeld soll nicht nur den Unsicherheiten engegenwirken, sondern vielmehr zu einer Vergrößerung des messbaren Himmelsabschnitts und des zugänglichen Energiebereichs beitragen und heutige Forschungsziele vorantreiben. Das hybride Detektorfeld wird sich über den Fußabdruck der IceCube Oberfläche erstrecken und insgesamt 32 Stationen mit jeweils acht Sintillatordetektoren und drei Radioantennen umfassen.
Diese Arbeit konzentriert sich auf die Szintillatordetektoren und definiert das Ziel einer Energiekalibrierung. Diese wird durch die Nutzung von radioaktiven Quellen realisiert und nimmt eine wichtige Rolle in dem gesamten Prozess der Szintillator-Kalibrierung für die Messung von Luftschauern ein. Die verwendeten Proben strahlen mit kleinerer Energie, als für den Energiedeposit von Einzelteilchen aus der kosmischen Strahlung angenommen ist und spiegeln so ihr charakteristisches Spektrum in den Messdaten wider. Im Gegensatz zum Energiespektrum der radioaktiven Quellen, ist die Energieauflösung der Szintillatoren durch bedeutende Unsicherheiten geprägt. Das Positionieren der aktiven Quellen an verschiedenen Stellen um den Detektor und die Durchführung von variierenden Messungen ermöglichen Rückschlüsse auf die Beziehung zwischen dem gemessenen digitalisierten Signal (ADC-Kanal) und dem korrespondierenden Energiedeposit zu. Die Abhängigkeit zwischen ADC-Kanal und Energiewert wurde in zwei Messreihen mit einer sich unterscheidenden Auswahl von radioaktiven Proben, sowie einem leicht veränderten Versuchsaufbau bestimmt und bestätigt. Zur Vorbereitung auf die Messungen werden die Randbedingungen sowie äußere Einflüsse untersucht. Die Messungen wurden unter Verwendung der drei radioaktiven Proben Natrium 22, Cäsium 137 und Cobalt 60 durchgeführt. Die Streuung der charakteritischen Compton-Kanten in den ADC-Spektren verrursacht durch die radioaktive Strahlung werden für verschiedene Bedingungen gemessen und ihre Position im Ladungshistogramm durch einen angepassten Fit bestimmt. Dabei wurde die Intensität der Compton-Kante als 70% der Intensität des durch einen Gauß-Fit gefundenen Höchstpunkt im Ladungshistogramm angenommen. Dies ermöglicht die Zuweisung des jeweiligen ADC-Kanals zu einem spezifischen Energiewert und die Demonstration einer linearen Korrelation. Um schließlich die gefundene Linearität zu prüfen, wurde für jede Messung der Energiewert des Signals kosmischer Teilchen ermittelt und festgestellt, dass sich dieser in den erwarteten Energiebereich einfügt.

Contents

1. Introduction **1**

2. Cosmic rays and extensive air-showers **3**
2.1. Cosmic rays . . . 3
2.2. Air-showers . . . 4
2.3. Detection methods . . . 6
2.3.1. Particle detectors . . . 6
2.3.2. Air Cherenkov light detectors . . . 8
2.3.3. Radio detectors . . . 8
2.3.4. Fluorescence detectors . . . 8

3. The IceCube Neutrino Observatory **11**
3.1. IceCube In-Ice Array . . . 11
3.2. IceTop . . . 13
3.3. IceCube Surface Array Enhancement (SAE) . . . 14
3.4. IceCube-Gen2 . . . 14

4. Surface Array Enhancement **17**
4.1. Overview . . . 17
4.2. The Central DAQ . . . 17
4.3. Radio detectors . . . 17
4.4. Scintillation detector . . . 18

5. Calibration with radioactive sources **23**
5.1. Decay processes . . . 23
5.2. Radioactive sources . . . 24
5.2.1. Beta sources . . . 24
5.2.2. Neutron source . . . 26
5.3. Experimental setup . . . 26
5.3.1. 2022 measurements . . . 28
5.3.2. 2023 measurements . . . 29

6. Data preparation and analysis **31**
6.1. Preparation . . . 31
6.1.1. Cable analysis . . . 31
6.1.2. Analysis of the radioactive source positions . . . 32
6.1.3. Threshold choice . . . 34
6.1.4. Panel absorption . . . 34

6.2. Data preparation . . . 35
6.3. Fit functions . . . 36
6.3.1. Fitting the MIP peak: Gaussian and Landau . . . 36
6.3.2. Fitting the Compton edges: Modified Gaussian and Gaussian . . . 37

7. Calculation of the ADC-Energy-Relation **41**
7.1. Fitting results . . . 41
7.1.1. Data set 2022 . . . 41
7.1.2. Data set 2023 . . . 44
7.1.3. Peak identification . . . 49
7.1.4. ADC channel assignment . . . 50

8. Summary and outlook **57**

Bibliography **61**

A. Appendix **65**
A.1. Cable tests . . . 65
A.2. Threshold choice . . . 65
A.3. Experimental setup . . . 65
A.4. Fit results . . . 65
A.4.1. Without source . . . 65
A.4.2. Sodium22 . . . 65
A.4.3. Cesium137 . . . 73
A.5. Linear coherence . . . 73
A.5.1. Linear regression - 2022 . . . 73
A.5.2. Linear regression - 2023 . . . 76

1. Introduction

The existence of the *cosmic rays* was already confirmed in the beginning of the 20th century [1]. Ever since the study of cosmic rays evolved, bringing promising experiments and discoveries to the table of multidisciplinary astrophysical researches. Nevertheless a lot of substantial questions remain unsolved, even after more than a 100 years. Especially the origin of high-energy cosmic rays is mainly undiscovered. The determination of their source is challenging as cosmic rays cause a shower of secondary and tertiary particles by passing the Earths atmosphere. These particles generated by a simple high-energy cosmic ray are defined as *air shower* and spread over hundreds of meters [2]. The detection of these air showers as well as the gaining of information about the source, demands detectors over an extensive area. The IceCube Neutrino Observatory, which is located at the geographical South Pole, fulfils this criteria regarding its large volume. It has a scale of one cubic kilometer and an in-ice detector as well as an detector array on the surface, called IceTop [3]. The In-Ice array of IceCube is composed of 86 strings with entirely more than 5000 optical sensors, which trace the Cherenkov light, generated by high energy particles passing through the ice. IceTop consists of 81 stations, each comprises two Cherenkov ice tanks and serves as a Veto for an event measured by the in-ice detector and moreover as an independent cosmic-ray detector [4]. Furthermore, an extension of the surface detector is planned: *the Surface Array Enhancement (SAE)*. It is planned to be built of 32 stations, each consisting of eight scintillation detectors as well as three radio antennas [5]. The main purpose of the hybrid detector array lays in the reduction of the systematic uncertainties of IceTop, but nonetheless it also enables an improvement of the accuracy and the sky coverage for high-energy cosmic rays [6]. IceCube is the first detector detecting neutrinos with galactic and extraglactic origin and promises further discoveries. Especially the foreseen expansion to IceCube Gen2, where the Surface Array Enhancement constitutes the baseline design of the Gen2 surface array, might widen the scientific possibilities in cosmic-ray physics. The already for the SAE deployed prototype station was tested as well as analysed and represents an important part in the realisation of the Surface Array Enhancement [5].
This thesis focuses on the Surface Array Enhancement, especially the scintillation detectors. In order to get a deeper understanding of their functionality, respectively their comparability, an energy calibration was proceeded, which is an important part in the entire calibration chain for the scintillators at the production level for the measurement of air showers. Further, three varying radioactive sources and several measurement series were utilised to proof the required linear relation between the digitized light signal (ADC-channel) of the scintillation detectors and the corresponding deposited energy due to the particle interaction. First of all, chapter 2 presents an overview on cosmic rays, their discovery as well as the present topics of researches. Furthermore, air showers are discussed and the various detection methods as particle detectors, air Cherenkov light detectors,

radio detectors and fluorescence detectors are explained. Chapter 3 introduces IceCube as Neutrino Observatory with the In-Ice Array, IceTop, the Surface Array Enhancement and IceCube-Gen2 with its technical setup and functionality. Chapter 4 focuses more detailed on the Surface Array Enhancement, explains shortly the central DAQ as well as the radio detectors and goes into detail for the scintillation detectors. In chapter 5 the fundamental idea of the calibration is explained by presenting the utilised active sources, Na22, Cs137 and Co60, their decay processes and the experimental setup. Furthermore it is ascertained why the scintillators exclusively measure the characteristic Compton edges of the sources. Chapter 6 explains the preparation of the data as well as the methods for the following data analysis. Finally, in chapter 7 the measurement results are collected and the linearity between ADC-channel and energy deposit value is built. This linear dependence is interpreted considering the various possibilities of the Compton edge determination as well as the measurement uncertainties and the role of the simple particle (MIP) peak. Chapter 8 resumes the thesis objective as well as its outcome and gives an outlook for further investigations and opportunities.

2. Cosmic rays and extensive air-showers

2.1. Cosmic rays

Highly energetic charged particles, with an energy range in the orders of GeV up to 10^8 TeV and an extraterrestrial nature are called *cosmic rays* [7]. They originate during galactic and extragalactic processes like star formation, supernova explosions and stellar evolution. These rays predominantly consist of protons or atomic nuclei [2] and their discovery is dated back to the beginning of the 20th century. Their initial detection was based on the observations of Domenico Pacini, who investigated the ionization of an electroscope, as well as Victor Hess, who ascertained a radiation, that was never seen before, during one of his famous balloon flight experiments. This radiation was later named *cosmic radiation* [1, 8]. With its discovery many new subareas in physical researches emerged and cosmic ray research became a multidisciplinary field. This includes elementary particle processes, nuclear physics, plasma physics, astronomy and thermodynamics etc. [9]. However, the exact origin of cosmic rays is still one of the major points of investigation. The determination of the source of cosmic rays is increasingly challenging due to acceleration of the emitted particles not only by the source itself, but also by the interstellar medium. During the propagation through space the particles might either interact with interstellar matter, magnetic fields or radiation fields, which could result in loss of energy or acceleration to an even higher energy level. The charged particles are accelerated in the sources and arriving at the Earth's atmosphere are called *primary* cosmic rays [10]. After passing the atmosphere, interacting and scattering with the atomic nuclei in the atmosphere, they produce secondary and tertiary particles. Therefore, almost none of the primary photons, electrons and nuclei reach Earth's sea level. But analysing and interpreting the energy spectrum and the composition of the air-showers can reveal information about these primary cosmic ray particles and their origin [9].

The energies of the primary particles vary by multiple orders of magnitude, ranging from several MeV to about 10^{14} MeV. This energy spectrum represents particles produced in our Solar System as well as the cosmic rays with an extragalactic origin and energies higher than any human built accelerator have ever reached. Various experiments using direct and indirect cosmic ray detection realise the study of their energy spectrum, specialized on a certain energy range. Figure 2.1 shows the intensity of cosmic rays measured by such different experiments. The spectrum roughly follows a power-law distribution over many orders of magnitude with changes in the exponent due to changes in the source population or the maximum energy of acceleration mechanisms or propagation effects. The cosmic ray flux is scaled by a factor of $E^{2.6}$ to visualise the spectral features more clearly. One can determine three points of interest in this spectrum, where the slope of the

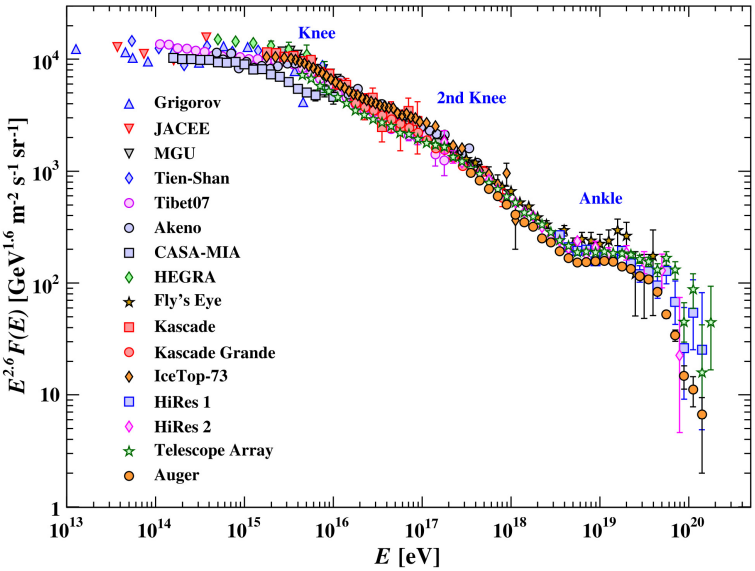

Figure 2.1.: The energy spectrum of cosmic rays measured in different ground-based experiments. The plot is taken from the Particle Data Group regarding cosmic rays [12].

spectrum changes visibly. These transition points are called the *knee* (estimated at 3 PeV), the *second knee* (at roughly 100 PeV) and the *ankle* (at approximately 5×10^3 PeV) [11]. These transition points describe the varying composition of the cosmic ray, consisting of nuclei of various heavy elements. The contribution from the light elements decreases at the knee, the one from the heavy elements at the second knee. Between the second knee and the ankle, the galactic sources transits into the extragalactic [5].

2.2. Air-showers

When a primary cosmic ray particle interacts with the Earth's atmosphere it scatters or decays into secondary particles resulting in what we refer to as *air-shower*. The particleprofile of an air shower follows

$$N(t) \sim t^{\alpha} exp(-\beta t), \tag{2.1}$$

where $t = \frac{x}{X_0}$ describes the depth of the shower, measured in terms of their radiation length and α and β are free fit parameter. The atmosphere has a depth of about 27 radiation length, which indicates, that a primary cosmic ray requires at least an energy of 100 TeV to realise a measurement of the air shower at sea level. The coherence between the particle amount N and the primary energy can be roughly displayed through

$$E_0 = 10^{10}\ \mathrm{N}, \tag{2.2}$$

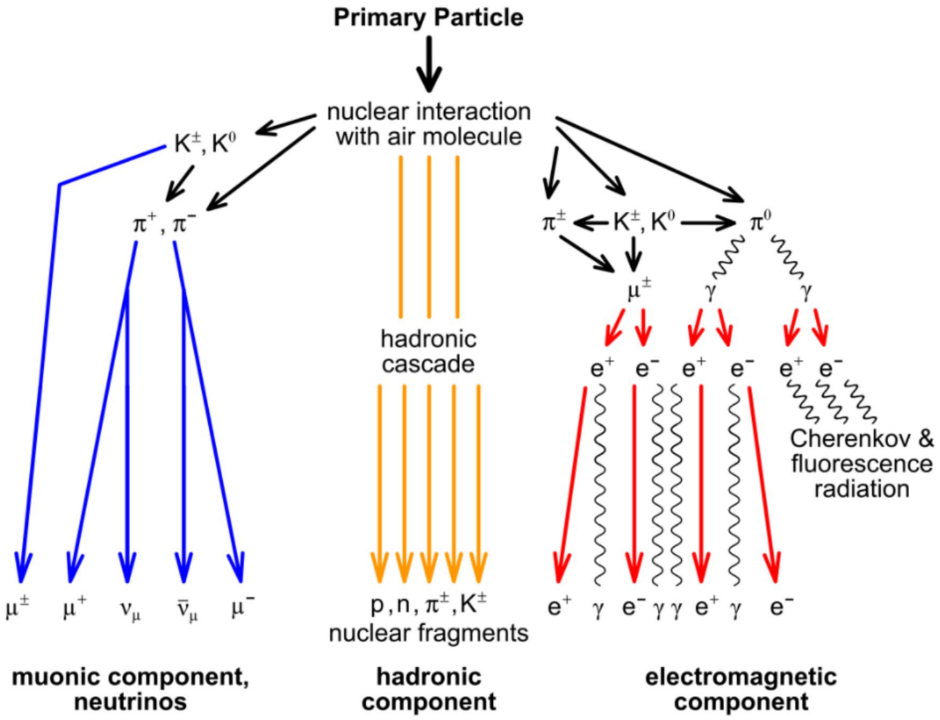

Figure 2.2.: Illustration of an air-shower initiated by a high-energy cosmic ray with the different cascade components: hadronic (yellow), electromagnetic (red), muonic and neutrino (blue) parts [4, 14].

where E_0 is described in eV [13]. These showers can be mainly differentiated into the hadronic, the electromagnetic and the muonic components. In figure 2.2 the scheme of an air-shower with different cascade components is illustrated.

The first hadronic interaction of the primary cosmic rays can produce several energetic hadrons, mainly pions and kaons. Pions and kaons are unstable and decay in the air rapidly. The resulting particles are comparatively stable and lighter. Pions represent the lightest mesons and are therefore produced in a large number in the hadron cascades. Kaons on the other hand are only produced with a probability of roughly 10 % compared to pions. The pion appears in two forms: charged and uncharged [9]. The neutral pion is less stable and decays into two photons, which initiate electron-positron pair production or ionization, and therefore continue the electromagnetic cascade. The charged ones can either interact again with atomic nuclei of the atmosphere and continue the scattering of the hadronic cascade or decay into a muon and neutrino pair [11]. Muons produced through pion decays make up the biggest part of the muonic component that arrives at sea level with a muon flux of one particle per cm^2 per minute. Thus the muon spectrum reflects the pion spectrum directly [10]. Apart from the charged particles, neutrinos are produced in the decays of pions, kaons and muons. One can differentiate between three kinds of neutrinos: electron neutrinos, tau neutrinos and muon neutrinos. Muon neutrinos, mainly emerging from the decay of muons and kaons, appear to dominate [2].

2.3. Detection methods

The detection of air-shower particles, especially neutrinos, is challenging because of their very low probability of interaction. This brings up the necessity of using large-volume detectors with good energy, time and angular resolution. The location of air-shower detectors depend on the energy range for the shower which is aimed to be observed. For a lower energy value (less than 100 TeV) a high altitude location is preferred, where the observation level gets closer to the shower maximum. On the other hand for higher energies is expected to be at smaller altitudes, to minimize the observation of showers before they have reached their maximum development [10].

The classical technique for detection used at sea level can be broadly divided into four categories: *Particle detectors, air Cherenkov detectors, Radio detectors* and *fluorescence detectors*. These detector principles either detect air-shower particles directly (particle detectors) or measure the electromagnetic radiation which is generated by the electromagnetic component of the air-shower (air Cherenkov, Radio and air-fluorescence detectors) [6]. Scintillators are the most popular ionizing radiation detectors utilised in various experiments around the world. Beside the KASCADE-Grande experiment (Germany), also the Pierre-Auger-Observatory (Argentina), the Yangbajing Cosmic Ray Observatory (Tibet) and the Telescope Array Observatory (USA) consists of scintillation surface detectors. Likewise scintillation detectors also Radio detectors are utilised in combination with other techniques. Therefore, radio detectors are also applied at the IceCube Neutrino Observatory and the Pierre Auger Observatory. Particle Cherenkov detectors are found at the IceCube Neutrino Observatory as well as at the High-Altitude Water Cherenkov Observatory (Mexico). The High Energy Stereoscopic System (Namibia) as well as the Major Atmospheric Gamma Imaging Cherenkov Telescopes (La Palma) use air Cherenkov detectors. Among others, fluorescence detectors can be found at the Telescope Array experiment [15]. Figure 2.3 shows example pictures of a particle detector as well as a Radio, a Cherenkov and a fluorescence detector and figure 2.4 illustrates an overview over these main classical techniques.

2.3.1. Particle detectors

Particle detectors are the most widely utilized technique for air-shower detection. The functional principle is the sampling of air-shower particles with scintillators or water/ice Cherenkov counters. Particles generated through air-showers from primary cosmic rays can be detected through excitation in the scintillation material. Energetic particles interact with a volume of sensitive material leaving an energy deposit which creates energetic electrons and holes in the material. Through a radiative recombination of electrons and holes light is emitted. This light response indicates the kind of the incoming particle [20]. The Cherenkov detectors also have a similar working principle as scintillators. There, the key is to measure the radiation produced through the bypassing particles. In this case the focus lays on the Cherenkov radiation which emerges from the relativistic particles transiting a transparent medium [17]. In the Cherenkov tanks, either water or

Figure 2.3.: Examples of deployed detectors. A scintillation detector at the IceCube Neutrino Observatory (upper left), a Radio detector at the IceCube Neutrino Observatory (upper right), an air Cherenkov detector Major Atmospheric Gamma Imaging Cherenkov Telescopes (downleft) and the Fluorescence detector at the Telescope Array experiment (downright) [16, 17, 18, 19].

ice, Cherenkov radiation is emitted, if the speed of the charged particles is higher than the phase velocity of light in the medium. Thus detection via Cherenkov light is preferred for high energy particles [2].

2.3.2. Air Cherenkov light detectors

Air Cherenkov light detectors are sensitive to the electromagnetic component of an air-shower and allow a good determination of their primary energy. The charged particles can display higher speed than the speed of light in air and therefore emit Cherenkov light, which is further measured. Air Cherenkov light detection is mostly used by the investigation of high energy neutrinos and represents an established technique for estimation of the primary particle type. Nevertheless it is also used for photon-induced air-shower physics, because of its good separation and direction analysis. The intensity of the Cherenkov light scales linearly with the shower energy. Thereby the detection of air Cherenkov light also yields a measurement of the air-shower energy. Furthermore the position of the air-shower maximum can be reconstructed. However, air Cherenkov detectors rely on the exterior circumstandes such as good weather and clear sky, which limits the measurement time of these detectors [6].

2.3.3. Radio detectors

Radio detectors are only sensitive for the electromagnetic component of the air-shower. The radio technique has an energy threshold of about 100 PeV and yields precise information about the arrival direction, the energy, as well as a good estimation of the atmospheric depth of the shower maximum X_{max} and the mass composition. Especially in combination with other detectors, such as particle detectors [15].
Radio emission is mainly generated due to two mechanisms:

- The dominant *geomagnetic effect* creates an electric field by separating the electrons and positrons in the magnetic field. The number of electrons and positrons changes during the shower development inducing a variation in time of their drift, which leads to radio emission.

- The *Askaryan effect* describes the time-variation of the charge excess in the shower front of the air-shower. This leads to an ionization of the atmosphere which results in a shower of secondary charged particles and thus emits radio emission [10, 6].

2.3.4. Fluorescence detectors

The fluorescence technique lays as well on the emission of light and is just sensitive to electrons and photons. The light has its origin in nitrogen molecules that are getting excited through the passing of the air-shower. On one hand, fluorescence detection shows a comparatively small uncertainty regarding the absolute energy scale and a direct sensitivity to the position of the shower, but on the other hand it isn't very sensitive to the muonic component of the shower as the radio emission and depends on a high threshold (about

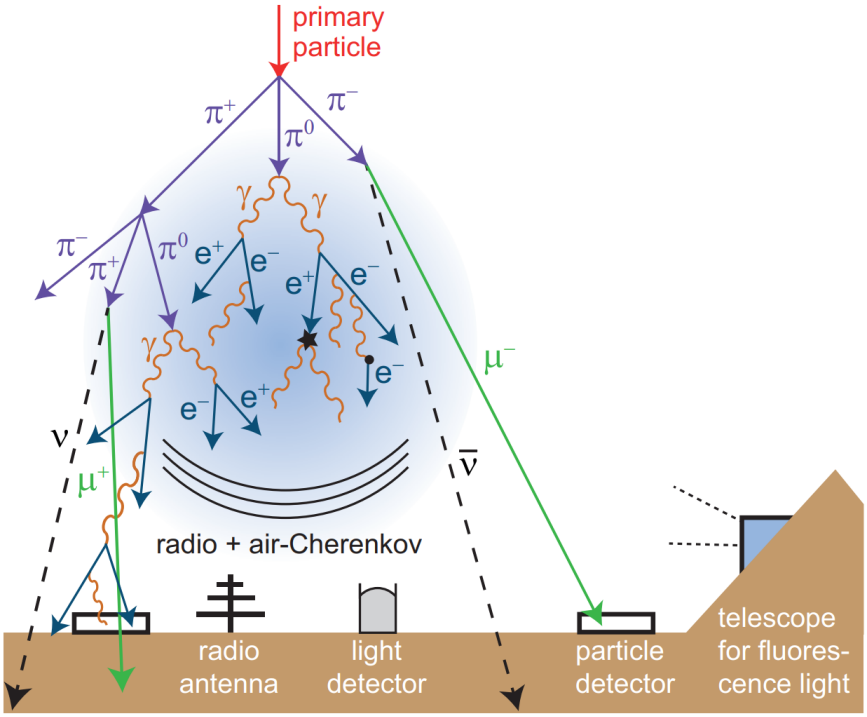

Figure 2.4.: Simplified schematic of an air-shower with its possible detection methods [6].

10^{17} eV [6]). Air-shower detection via fluorescence provides one main advantage. While the other techniques need large ground arrays to be built, the fluorescence technique has a large atmospheric volume just by a single detector and taking up only ranges from a few meter to a bit more than a kilometer [16]. This is explained by the directed Cherenkov radiation due to the isotropic emission of fluorescence.

3. The IceCube Neutrino Observatory

The IceCube Neutrino Observatory, hereafter called IceCube, is a high-energy neutrino detector located at the geographic South Pole. It has a scale of one cubic kilometer and is built into the ice. The detector mainly comprises of the In-Ice detector array, including Deep Core and the surface array, Ice Top. All modules together conspire to a detector which is able to observe air-shower particles in an energy range from some 100 TeV to about 1 EeV [21] and neutrinos up to a few PeV [22]. This qualifies IceCube as a multipurpose experiment regarding neutrino astronomy, the study of cosmic rays and further investigations of the high-energy universe. IceCube gains promising results, revealing the potential to explore the high-energy universe further.

The measurements done by the IceCube detectors provide information about the primary composition of the primary cosmic ray. For example air-showers induced by iron or proton carrying the same primary energy can be differentiated through their amount of muons. Iron-induced showers are more muon-rich than proton-induced showers and therefore will result in a greater overall deposit of Cherenkov light in the In-Ice detector. On the other hand, proton-induced showers with the same primary energy are more likely to have high energy muons, which can create larger local energy depositions. According to that proton-induced showers are expected to create fewer but higher-energy and iron-induced shower more lower-energy losses in the in-ice detector [23].

3.1. IceCube In-Ice Array

The IceCube In-Ice Arrray consits of thousands of detectors underneath the ice, tracing the Cherenkov radiation from highly energetic particles. These detectors, Digital Optical Modules (DOMs), observe the pattern of the Cherenkov light, which is emitted by charged leptons created through the reaction of the high-energy particles with the molecules of the ice [23]. The setup and dimension of IceCube is seen in figure 3.1 with 86 strings building the IceCube In-Ice Array. Each string suspends 60 DOMs, bringing the total modules of 5160 in number. These are deployed within a hexagonal footprint reaching a total depth of 2450 m [22]. Figure 3.2 presents the installation of a DOM on one of the strings.

DeepCore

A sub-array of the IceCube In-Ice Array, DeepCore, is formed by a subset of strings that are located in the center of the array and have a higher density of the DOMs. The configuration of the strings are deployed more compactly, with a horizontal separation of about 70 m instead of 125 m and a vertical spacing of 7 m instead of 17 m [27]. This is instrumented to achieve a lower neutrino energy threshold which creates the opportunity to study neutrino

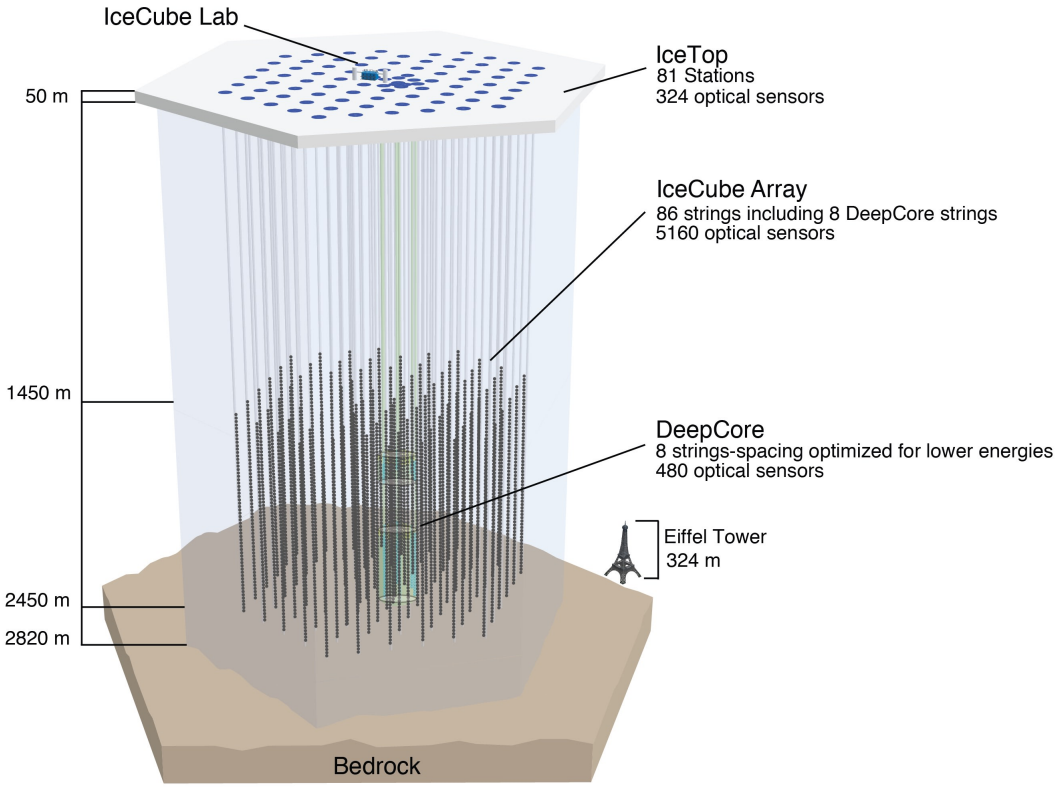

Figure 3.1.: Schematic of the IceCube Neutrino Observatory [24].

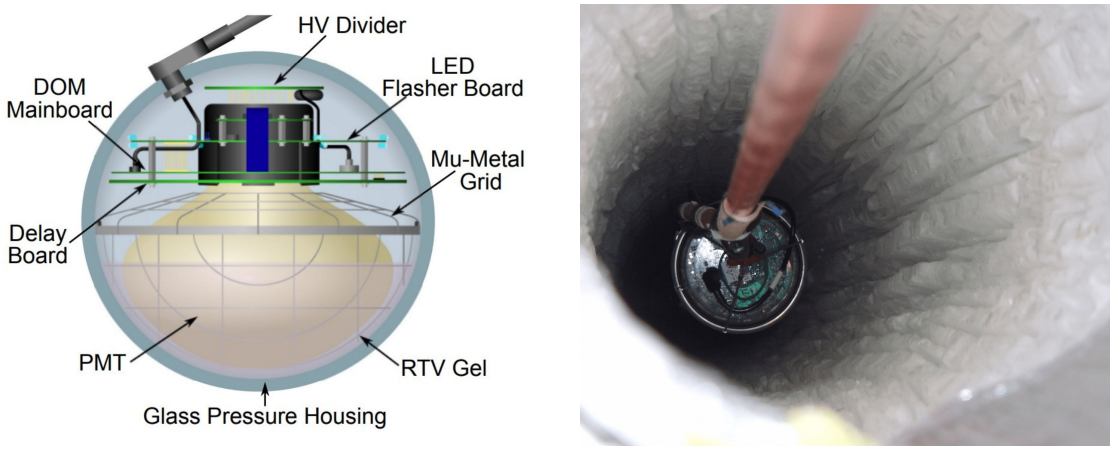

Figure 3.2.: Schematic structure of a DOM on the left hand side and on the right hand side a DOM descending for the In-Ice Array into a borehole of approximately 60 cm diameter [25, 26, 21].

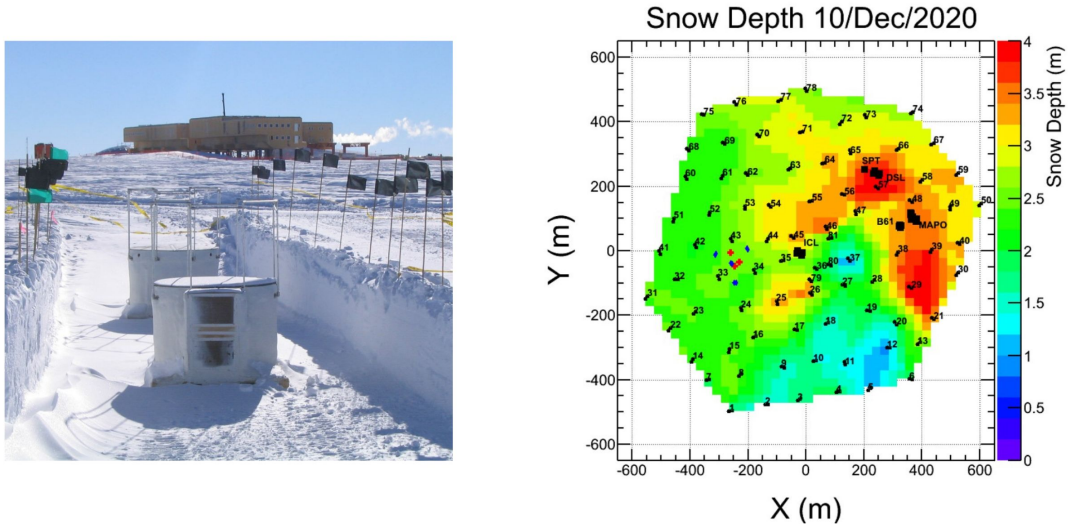

Figure 3.3.: Example of two ice-Cherenkov tanks deployed in a distance of 10 m. On the right hand side a plot of the snow accumulation at the surface array of IceCube, IceTop. [5].

oscillations [22]. These energies, laying between 10 GeV and 100 GeV, can furthermore be assigned to neutrinos from dark matter annihilation or Galactic supernovae [22].

3.2. IceTop

Apart from the In-Ice Array, there also exists a surface array comprising of 162 ice-Cherenkov tanks placed on the surface of the snow [21]. Figure 3.3 shows a picture of an installed Cherenkov detector and figure 3.4 an illustration of its structure. IceTop is used as a veto against astrophysical background for the In-Ice Array as well as a calibration detector for IceCube. The veto helps filter the downward-going neutrinos from the abundant background of cosmic ray induced muons and neutrinos and works moreover as coincidence method for the ratio of deep signal to surface signal which can be used to find the relative fraction of heavy cosmic rays [21]. Moreover it presents an opportunity for cosmic ray physics as it detects air-showers from primary cosmic rays in an energy range of a few hundred Tev to EeV [28]. The sensitivity of the IceTop allows to cover the characteristic *'knee'*-region of the energy spectrum, where a transition from cosmic rays with galactic origin to cosmic rays with an extra-galactic origin occurs. Nevertheless the non-uniform height of the snow layer deposited on the Cherenkov tanks over the period of a decade now exacerbates the measurements. Because the different amount of snow attenuates the detected signal variably, the uncertainties in the reconstruction of the air-showers increases.

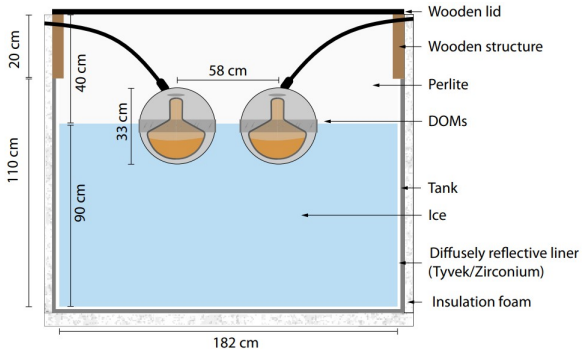

Figure 3.4.: Illustration of one ice Cherenkov tank. Two DOMs read out the light signal [21].

3.3. IceCube Surface Array Enhancement (SAE)

IceTop is able to measure the cosmic rays arriving from the galactic and extra galactic transition region. But the uncertainties increase due to the snow accumulation. To counteract these snow contributions and improve cosmic ray studies, a new surface enhancement consisting of two types of detectors will be installed along the footprint of IceTop [29]. By this increment the energy threshold for air-shower measurements will be lowered and the separation of the electromagnetic and muonic component will be improved. This enhancement array will comprise 32 stations each containing four pairs of scintillation detectors and three dual-polarized radio antennas. All parts are controlled by a central data-acquisition (DAQ). A conceptual layout is shown in figure 3.5. To prevent snow accumulation influences all the modules will be elevated installations [28]. This thesis focuses on the scintillation detectors, which will be further elaborated in chapter 4. For a detailed description of Radio detectors, refer to [19].

The prototype station

After a few revisions over some deployment seasons, the complete prototype station has been operational at the South Pole since 2020 [29, 4]. The pictures in figure 3.6 show an installation of parts of one station.

The Surface Enhancement will mitigate the uncertainty of the snow accumulation, enable studies of the attenuation effect regarding high-energy air-showers as well as an improvement of the energy sensitivity. This will allow also measurements of low-energy air-showers. The added radio antennas enhance the accuracy and sky coverage for high-energy cosmic rays.

3.4. IceCube-Gen2

In order to improve the capabilities of IceCube as neutrino detector the next-generation observatory is foreseen. IceCube-Gen2 will include the initial detector at the south pole as well as the enlarged detector's volume of eight cubic kilometers as well as a widespread

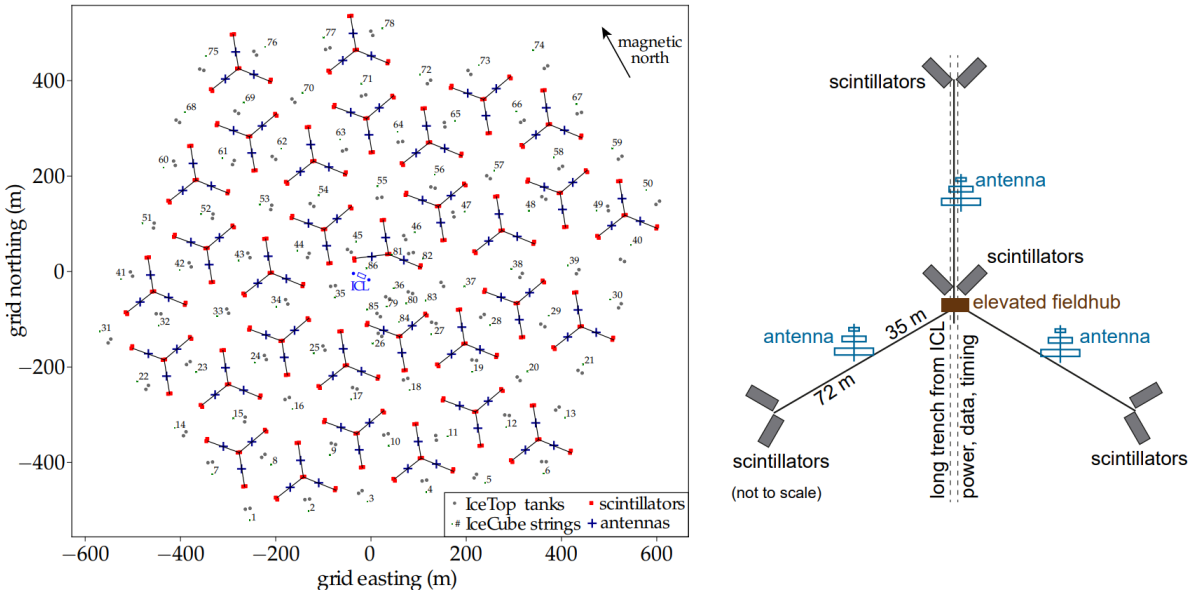

Figure 3.5.: The outline of the surface enhancement array with one of the stations illustrated on the right hand side. The DAQ is located in the center, elevated in a fieldhub. The Radio antennas are placed along each connection line between the scintillators [28].

Installation of a scintillator module. Installation of a radio antenna.

Figure 3.6.: Examples of deployed modules at the prototype station [3].

in-ice radio array and the extension of the Surface Array Enhancement. This will lead to an increment of the annual rate of observed cosmic neutrinos by a factor of ten compared to the status quo. Moreover it is expected to also be able to detect sources much more fainter than the ones that are observed now and to extend the energy range capacity. IceCube-Gen2 will mainly investigate the acceleration and propagation of cosmic rays by multi-messenger observations and advance the knowledge of the high-energy universe [30].

4. Surface Array Enhancement

4.1. Overview

As mentioned in the previous chapter, the Surface Array Enhancement (SAE) will consist of 32 stations [28], each of eight scintillation detectors and three radio antennas, as well as one central data acquisition system (DAQ) which combines the signal input from the scintillation detectors and the radio antennas [29]. This chapter will give a more detailed description for the enhancement components.
Figure 4.1 shows the detection chain in a station of the SAE. The central DAQ is deployed in the field and linked to the general IceCube surface DAQ installed at the IceCube Laboratory (ICL). It supplies power, communication and timing to the station. The timing is provided by a White Rabbit (WR) switch with a sub-nanosecond accuracy located in the ICL. The White Rabbit Lite Embedded Node (WR-LEN) is included in the fieldhub passing the timing from the WR on to the scintillation detectors. The signals of the scintillation detectors are already digitized in the panels using the MicroDAQ (uDAQ) and then passed to the central DAQ. Moreover, the scintillation detectors trigger the readout of the signals of the radio antennas.

4.2. The Central DAQ

The central DAQ per station is the main supplier of power and communication and timing to the station. It consists of two main components: the WR and the ***T**ransportable **A**rray for e**X**tremely large area **I**nstrumentaion studies* (TAXI) [31]. The WR is responsible for the timing. It is provided by the switch located at the ICL and the node (WR-LEN) in the DAQ box. The TAXI is responsible for the communication with the detectors and the transfer of their data to the surface DAQ at the ICL) [32].

TAXI consists of a mainboard, which is the basis for the data acquisition as well as a fanout board for the connection to the scintillators and their power supplies. Three radio TADs provide the electronics and connection to the radio antennas [31]. Figure 4.2 and 4.3 show the central DAQ. A detailed description is given in the schematic figure 4.3.

4.3. Radio detectors

Each station consists of three dual polarised Log-Periodic Dipol Array (LPDA) antennas connected to the central DAQ. The LPDA antennas, developed by the SKA collaboration, cover a range of 50 MHz to 650 MHz [5]. The region of interest for the IceCube measurements lays between 70 MHz and 350 MHz. Nevertheless the exact band is chosen

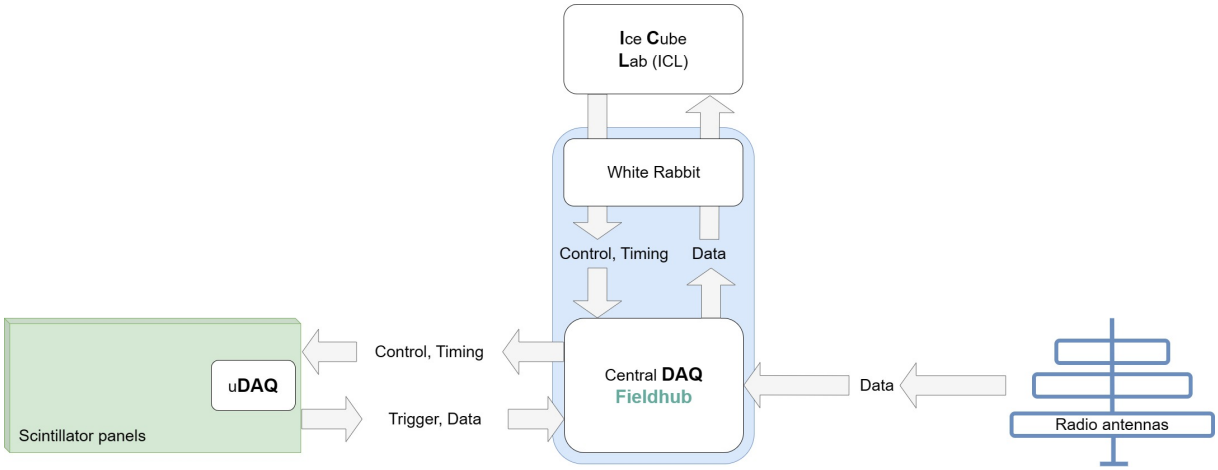

Figure 4.1.: Overview of the detection chain of one SAE station including the connections between scintillator and radio data to the ICL [5].

differently for each science case using digital filters. For instance the band of 110 MHz to 190 MHz allows the lowest threshold for cosmic ray showers in a certain angle. At the South Pole the radio background is generally low, which provides a good sensitivity to showers with weaker radio emission. Moreover the radio antennas will enable full sky coverage for the SAE [28].

4.4. Scintillation detector

The scintillation detectors are mainly foreseen for the measurement of the muonic and electromagnetic component of the extensive air-showers. Especially of interest are the energetic air-shower muons, that count to the characteristic class of **M**inimum **I**onizing **P**articles (MIP) and display an energy loss through matter close to the minimum. Nevertheless the passing of MIPs through scintillation material causes atoms to emit light, which can be collected and measured [34]. This is independent of the energy of the muon as long as it carries a relativistic velocity.

Electronic energy loss

The mean rate of the energy loss through ionization and atomic excitation of the relativistic charged particles in the scintillation material is given by the Bethe-Bloch equation [35],

$$-\frac{dE}{dx} = Kz^2\frac{Z}{A}\frac{1}{\beta^2}\left[\frac{1}{2}\ln\frac{2m_e c^2\beta^2\gamma^2 T_{max}}{I^2} - \beta^2 - \frac{\delta}{2}\right]. \tag{4.1}$$

Here, T_{max} describes the maximum kinetic energy, Z the atomic number of the absorber, A the atomic mass of the absorber, z the charge of the incident particle, I the exictation energy, δ the density effect correction to ionization energy loss and K a constant. The

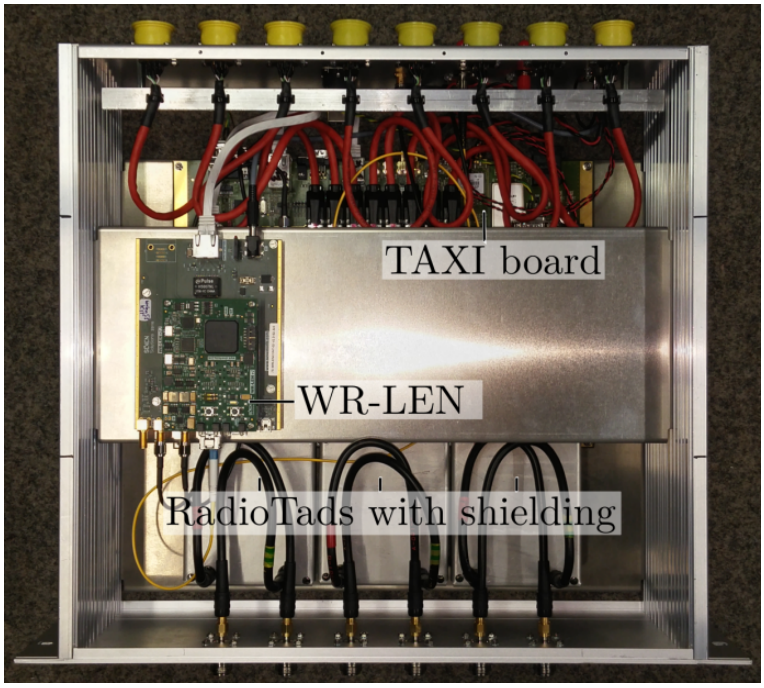

Figure 4.2.: Inside lateral view of TAXI DAQ including WR-LEN, fanout board (under the shielding) and the three radio TADs [5].

variables β, γ, c and m_e have their usual meanings [35]. Figure 4.4 shows the stopping power for positive muons in cooper, which at first increases with raising energy. The energy loss near the minimum belongs to the *minimum ionization* and characterises the stopping power of the **M**inimum **I**onizing **P**articles (MIP).

Scintillation detector

The scintillator detector subsystem contains plastic scintillator bars in combination with wavelength-shifting fibers for the collection and guidance of the light produced by a passing energetic particle. The read out goes along a light sensor, in this case a SiPM (Silicon Photo Multiplier) and the whole structure is sheltered by a mechanical construction, which is light-tight and can stand the harsh environment conditions at the Pole. The output of the SiPM is further digitized by the microprocessor based board called uDAQ [32].

The used plastic scintillators belong to the group of organic scintillators. Since by principle of operation, scintillation material converts kinetic energy to light, a high conversion rate is a good indicator of a favourable candidate. Moreover this conversion should show a linear character, resulting in light yield being proportional to the deposited energy. A good light collection is only ensured if the material is transparent to the wavelength of its own emission. Moreover the decay time of induced luminescence should be short, otherwise, no fast signal pulses can be generated [20]. Most of these criteria are fulfilled by the organic scintillation material used in the SAE plastic scintillators. The scintillation process is based on the emission of photon by the transfer of an excited molecule falling

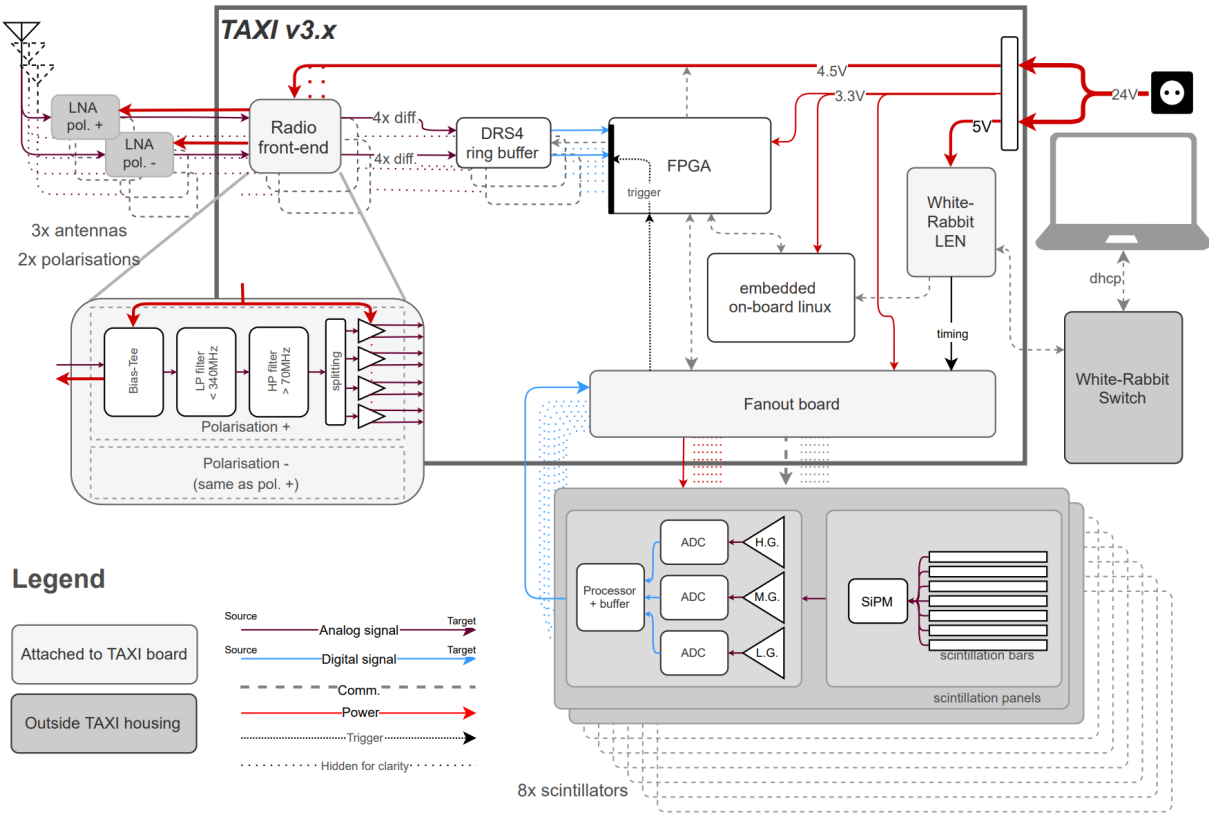

Figure 4.3.: Blockdiagram of the SAE electronics consisting of the TAXI board, the WR system, the radioTads, the fanout board, the uDAQs and the Low-Noise Amplifiers (LNAs) [33].

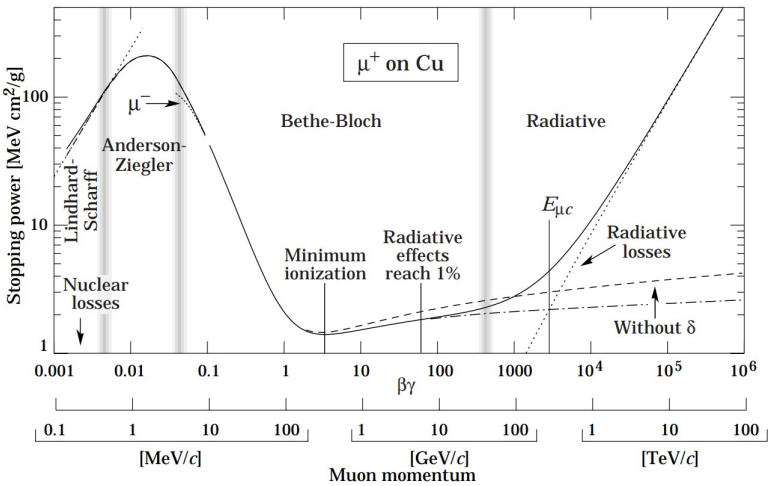

Figure 4.4.: Stopping power for positive muons over twelve orders of magnitude in kinetic energy [35].

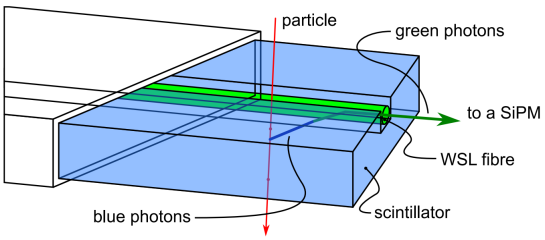

Figure 4.5.: Schematic of the interaction between crossing particle, scintillation material and wavelength shifting fibre [4].

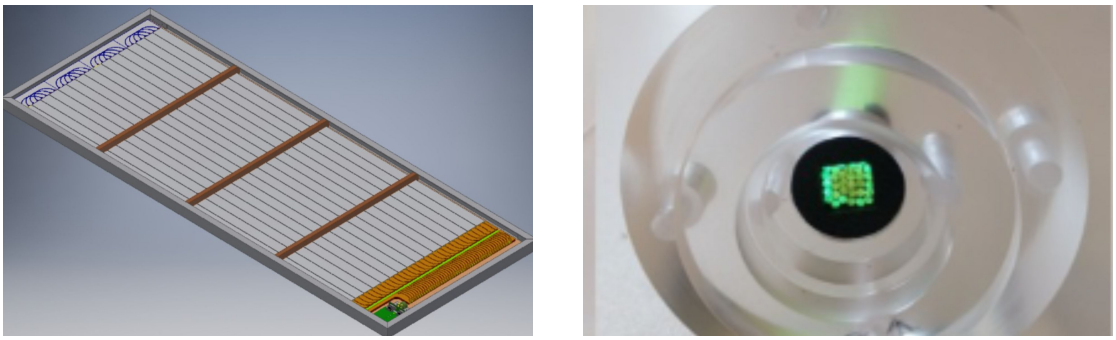

Figure 4.6.: Layout of the scintillation detector without the top plate on the left hand side and the wavelength fibers collected in the cookie on the right hand side [37, 38].

back into its ground electronic state. The molecule is further excited by the energy deposit of the energized particle that has crossed the scintillation material. In figure 4.5 the general schematic of the processes in a scintillation bar is illustrated.

The structure of the scintillator panel is orientated on a low-cost customisable geometry, constituted of detectors with a scale of 1.5 m^2 and a weight of less than 50 kg. Each detector comprises 16 plastic scintillator bars. These bars are 1 cm thick, 5 cm wide and 1.875 m long and are made of polystyrene with doping of 1 % PPO and 0.03 % POPOP. The whole bar is coated with a layer of TiO_2, which serves as reflector and prevents loss of photons. Each bar is traversed by two holes with a diameter of 2.5 ± 0.2 mm, which provide the space for wavelength-shifting fibers to pass through the scintillation material. They are produced by Kuraray (Y-11(300) [36]). They sum up to 16 fibers, which are routed with as less bending as possible and the same total length. Their readout is processed by a Silicon Photo-Multiplier (SiPM) with the size of 6×6 mm^2 [32]. The SiPM signals are further digitized by the scintillator uDAQ placed inside the panel. Figure 4.6 shows an illustration of the inside view of the detector as well as the cookie which couples the bundled fibers to the SiPM.

The SiPM along with a temperature sensor is placed on a circular circuit board, leading to the name *cookieboard*. The cookieboard is clued to the cookie with optical cement which is shown in figure 4.7. The SiPM used is produced by Hamamatsu and used to count the photons collected by the fibers. It is designed to have a lower dark count and to operate on low voltage [39].

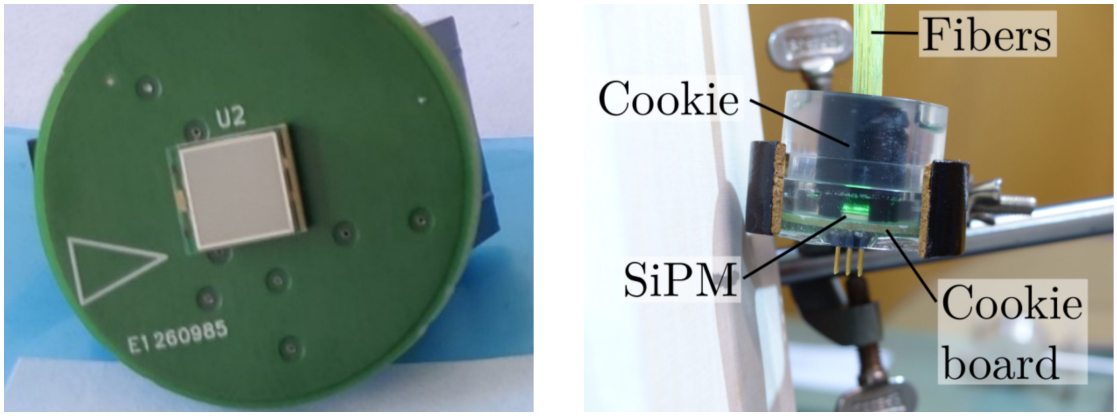

Figure 4.7.: View of the optical fiber connection to the SiPM which is placed on the cookie board on the right hand side and the front view of the cookieboard on the left hand side [5].

uDAQ

The uDAQ is a microprocessor based DAQ board and is only dedicated to a single sensor: the SiPM. The incoming signals are read out, digitized and then forwarded to the central DAQ. The bias voltage of the SiPM can be regulated through the uDAQ via a 12-bit digital-to-analog-converter (ADC), that is commanded by the name AUXDAC and lay in between AUXDAC 0 and AUXDAC 4095. The threshold of the SiPM readout is also set using a 12-bit ADC. The signal that the uDAQ receivs from the SiPM is passed through three gain channels and amplified by different factors. Afterwards the signal is shaped by a linear RLC network, which creates a signal which has a flat top for the period of approximately 100 ns and then goes back to the baseline within 500 ns. The amplitude of this signal is read out by sample- and-hold ADCs and saved as the measured charge of the hit. The ADC has a delay time, which build the possibility to also catch signals that occur delayed and maybe descend from a second particle interaction. A discriminator helps evaluate the time of the hit, where the time of the hit represents the time when the signal crosses the threshold.
This readout infrastructure allow two measurement modes: *hitbuffer* and *histogram*.

- **Histogram measurements:** The data for a fixed amount of measurement time is histogramed and saved on the uDAQ, allowing long measurements for calibration of the detectors. A histogram is generated for all three gain channels [40] .

- **Hitbuffer measurement:** A hitbuffer measurement saves the time of the hit, as well as the charge of the pulse for each gain, the time over the threshold and a flag to mark CPU triggered entries [32, 5].

5. Calibration with radioactive sources

The main objective of this thesis is to find a relation between the digitized light signal from the scintillators and the corresponding deposited energy due to the particle interaction. While the relation between energy deposit of muons, for example, and ADC channel contains still relevant uncertainties, the energy spectrum of various radioactive sources is widely studied and known. Hence the first conceptual attempt is a combination of a radioactive source with a spectrum observed by a scintillator. Through the positioning of the source in the vicinity of the scintillator panel the measured histogram gets modified to show the additional energy deposit of the gammas radiated by the source. Taking these characteristics into account with the measured position of the MIP a more concrete value for the energy range of the MIP peak can be deduced. This is important for verifying the theoretical and simulated predictions of the deposited energies in the scintillation material.

5.1. Decay processes

In order to determine the energy spectrum of radioactive sources, it is important to study the interaction of the gammas with the detector material. Three kinds of processes are possible: The *photoelectric effect*, the *Compton effect* and *pair production*.

Photoelectric effect describes the emission of electrons by an interaction of electromagnetic radiation with a material. When a gamma fully gets stopped in the material, it deposits all its energy and a *photo peak* emerges in the spectrum. Unfortunately the spectrum received by a plastic scintillator doesn't contain full-energy photo peaks. This is a consequence of the material of the scintillators constituting of low atomic number elements with weakly bounded electrons [41]. The incoming gamma shall be captured by the atom emitting one of its shell electrons and transfer all of the gamma's energy [42]. Due to that a considerable momentum is left over, which shall be admitted by the heavy atomic nucleus. Therefore, the bond of the shell electron needs a certain strength which is not provided by organic scintillators. The weakly bounded electrons are shoved away before the nucleus is able to gather the transferred momentum. Such being the case the plastic scintillators miss the photo peak completely [43].

Compton-effect describes the scattering of a gamma quanta after an interaction with a charged particle. The characteristics of the Compton effect align with the ones of an elastic collision. The energy as well as the momentum is preserved in this case. The passing gamma scatters with an electron and emits part of its energy [43]. The energy E_c received by the electron depends on the incidental angle Θ between the photon and a quasi-free electron [42],

$$E_c = E_\gamma \left(1 - \frac{1}{1 + \frac{E_\gamma}{m_e c^2}(1 - \cos(\Theta))} \right) \tag{5.1}$$

where E_γ is taken for the primary gamma energy and m_e for the electron mass. The Compton effect forms a continuous spectrum until the maximum energy $E_{c_{max}}$ is gained, which correspond to the angle of $\Theta = \pi$ and is called the *Compton edge*.

$$E_{c_{max}} = \frac{E_{gamma}}{1 + \frac{m_e c^2}{2E_{gamma}}} \tag{5.2}$$

Regarding the used plastic scintillation detectors, it stands to reason, that the characteristics induced by the active sources exclusively descend from the Compton edges [42].

Pair production of an electron and a positron emerges in the field of nuclear charge, if the primary energy is significant more than 2 $m_e c^2 = 1022$ keV. Regarding the energy ranges of gammas from sources used within the scope of this thesis their cross section for pair production is negligibly, so that no pair production is to be expected [43].

5.2. Radioactive sources

Two kinds of sources were considered for the measurements: beta sources and neutron sources. To identify the influence of the sources on the scintillation spectrum, the radioactive decay needs to lay in the energy range of the order of MeV. This covers the theoretical MIP value of $1.5 - 2.0$ MeV [44, 38]. Based on the availability of sources at the institute, within the radiation safety premise and this energy range, four suitable candidates were chosen: sodium-22, cobalt-60, cesium-137 and AmBe.

5.2.1. Beta sources

5.2.1.1. Sodium-22

Sodium-22 (Na22) is an unstable radioactive isotope with a half-life of 2.6 years. In the most common and probable case it undergoes the first positron emission by decaying into a beta plus particle with the energy of 546.7 keV and reaches ground state by emitting a gamma quantum with the energy of 1274.5 keV [45]. The corresponding two Compton edges are found at 340 keV and 1060 keV [46]. Figure 5.1 shows the energy levels with their probability as well as the decay spectrum.

5.2.1.2. Cesium-137

Cesium-137 (Cs137) is a radioactive isotope of cesium with an half-life time of about 30.05 years. Through beta emission it decays with a high probability to first 661.7 keV and then through the emission of photons to ground state [48]. The corresponding Compton edge is expected at 480 keV [46]. The decay pattern and spectrum is shown in figure 5.2.

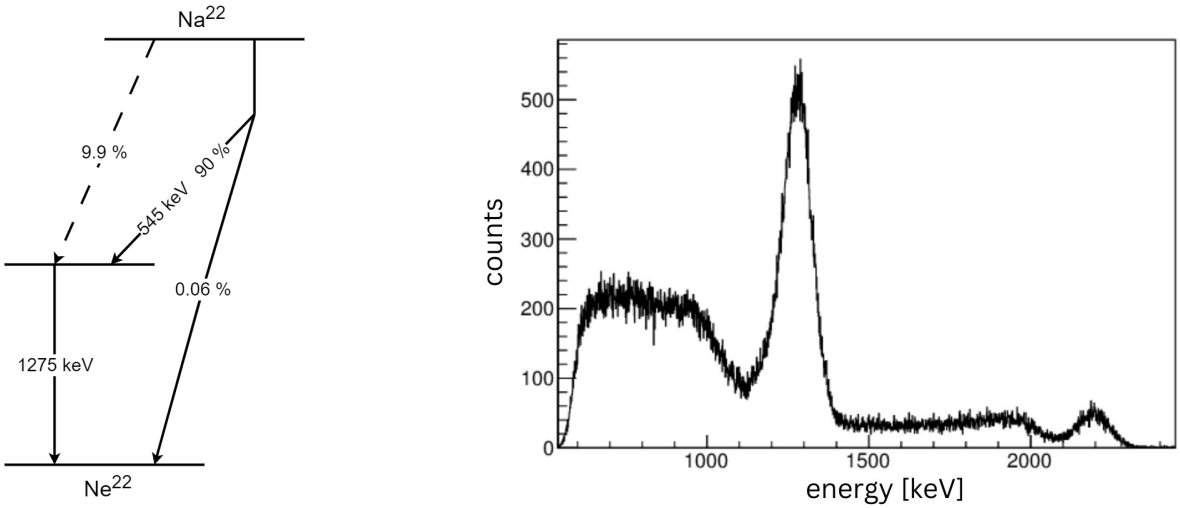

Figure 5.1.: Energy levels and spectrum of sodium-22 by beta and gamma decay [45, 47].

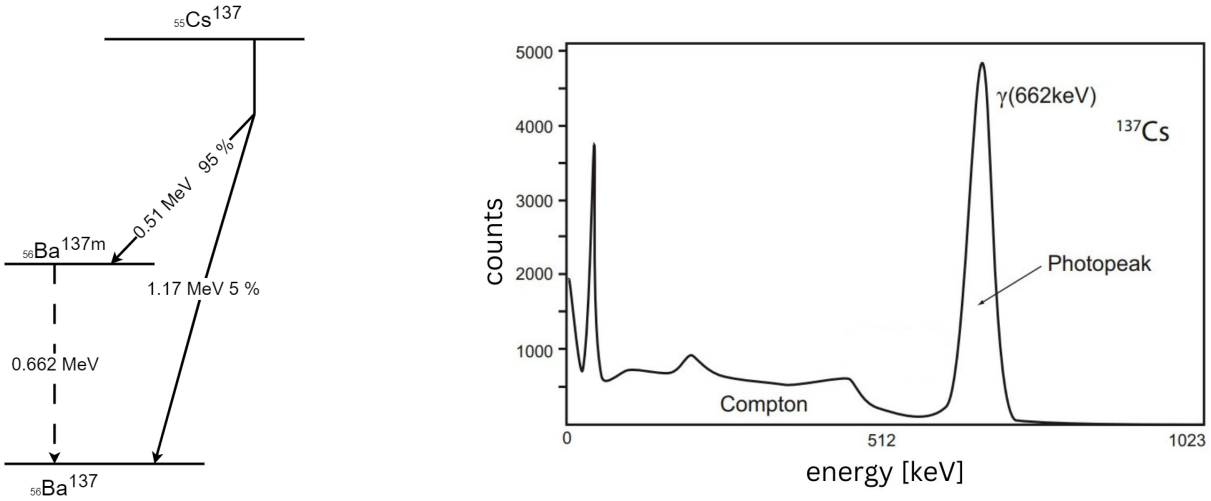

Figure 5.2.: Decay scheme and spectrum of cesium-137 [48, 15].

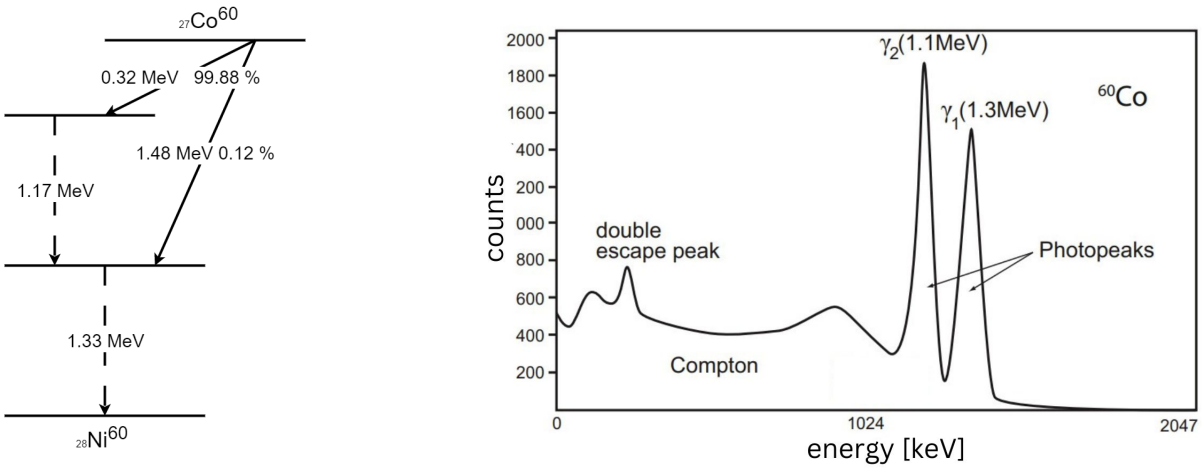

Figure 5.3.: Decay scheme and spectrum of cobalt-60 [48, 15].

5.2.1.3. Cobalt-60

The isotope cobalt-60 (Co60) of cobalt has an half-life time of 5.27 years and decays through emission of two gamma quanta to the main energy levels of 1173.2 keV and 1332.3 keV which is shown in figure 5.3 [49]. The two Compton edges of the photo peaks combine to one laying at 1040 keV.

5.2.2. Neutron source

5.2.2.1. Americium-Beryllium

Beside the radioactive sources that decay via beta and gamma emission another kind of source was tested. Americium beryllium (AmBe) is an amalgam containing two elements. It is declared as a neutron source, where the neutrons are generated by the beryllium after it absorbes an alpha particle emitted from the americium. The decay scheme is shown in figure 5.4. The three main peaks carry an energy of roughly 3.5 MeV, 4 MeV and 4.5 MeV [50].

5.3. Experimental setup

The characterization measurements were performed in two series:

- Measurements done in 2022 with Na22, Cs137 and AmBe
- Measurements in 2023 with Na22 and Co60

The basic setup structure for both measurement series doesn't differentiate significantly. The main distinction was in the *shielding* of the scintillation panels. The scintillation detectors are connected to the TAXI with installed DAQ and afterwards to a computer which allows to operate with the TAXI which is illustrated in figure 5.5. Earlier measurements

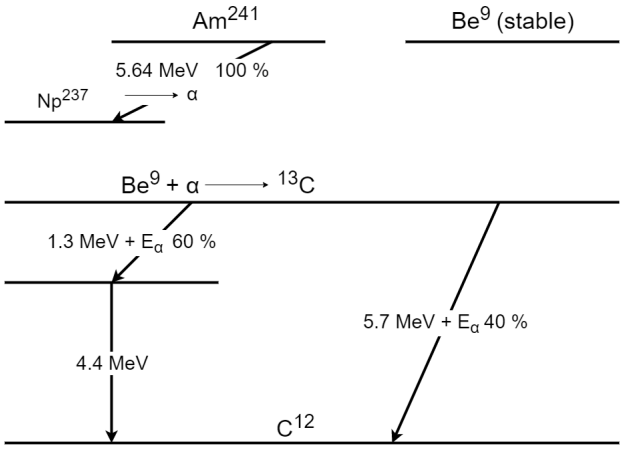

Figure 5.4.: Decay scheme of AmBe [51].

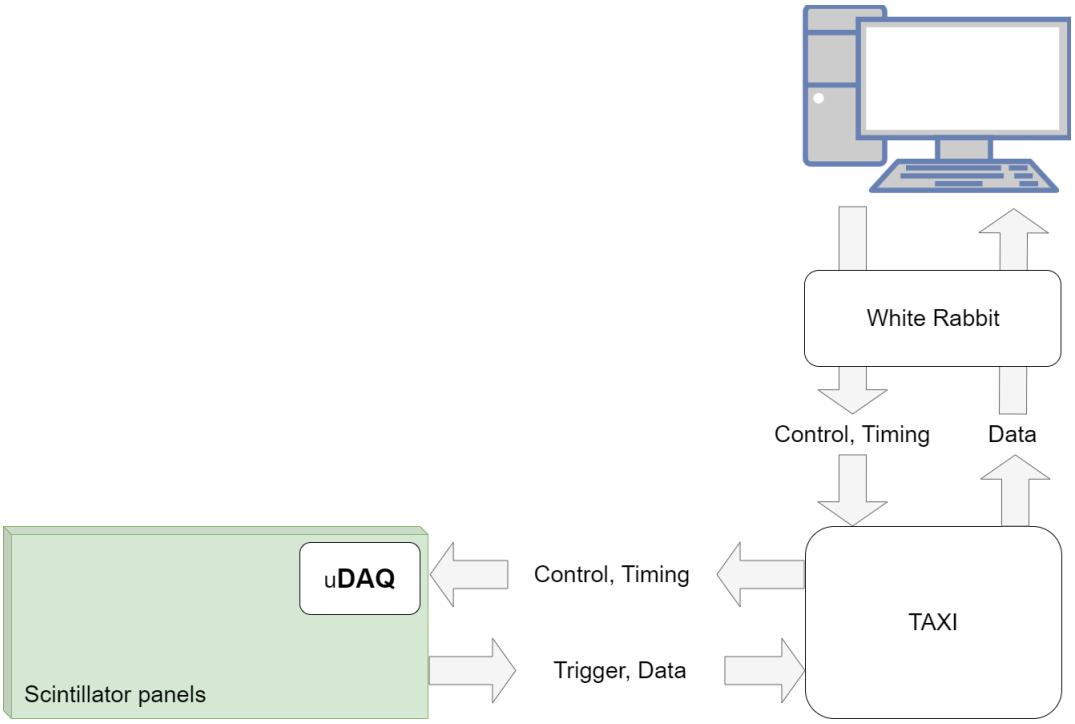

Figure 5.5.: Overview of the measurement chain at the KIT.

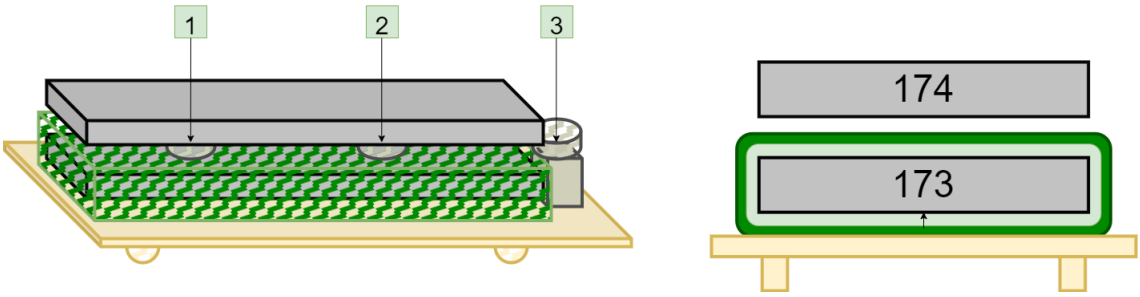

Figure 5.6.: Panel installation and variable positioning of the sources. The light green layer represents the neutron shielding composed of Boron Carbide plates, the darker green represents the gamma shielding composed of lead plates.

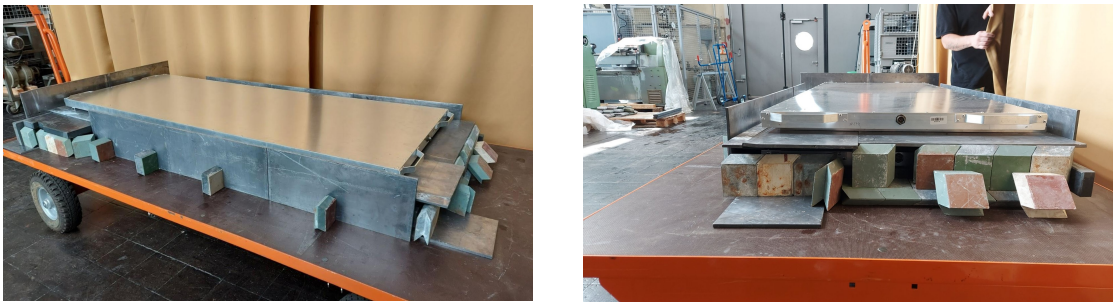

Figure 5.7.: Experimental setup with neutron and gamma shielding for the measurements done in 2022.

revealed a considerable background noise caused by the natural radioactivity mainly from the ground and concrete surroundings, which led to the shielding setup.

These sections discuss the setup in more detail, whereas the data analysis will follow in the next chapter.

5.3.1. 2022 measurements

The measurements done in 2022 utilised the sources Na22, Cs137 and AmBe and were performed with an outside temperature around 10°C. One of the scintillators, panel 173 (hereafter called panel 1), is covered by a neutron as well as a gamma shielding. The other one, panel 174 (hereafter called panel 2), is placed above. Both measurements were recorded at the same time. In figure 5.6 the arrangement is shown with three different positions of the sources varying on the horizontal axis. In addition a fourth position is explored only for the source Na22, placing the source in position one above panel 2. The fourth position was not pursued, because it didn't gain new information. In figure 5.7 two pictures show the experimental setup. The measurements in 2022 were performed mainly by an internship, but not fully analyzed. This thesis started after those measurements.

5.3.2. 2023 measurements

Since the scintillators are built to be uniform, moving the source horizontally on the detectors volume yields similar counts and spectra. This was also verified from the measurements conducted in 2022. Therefore, one central position was chosen for every measurement in the recent 2023 measurements. The analysis of the positions on the horizontal plain can be found in section 6.1.2. The only remaining difference lays in the positioning on the vertical axis and the temperature of approximately 20°C during the measurement. Therefore the source is either put above both panels, on top of the panel 2, or in between them. In addition position 3 describes the setup where Na22 is put in position 1 and Co60 in position 2 simultaneously. Figure 5.8 shows the panel installation with the source positioning as well as the shielding and figure 5.9 two pictures of the setup.

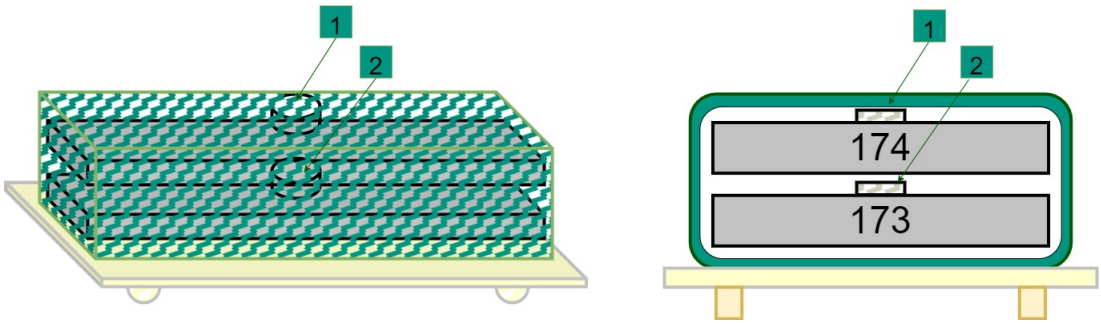

Figure 5.8.: Panel installation and variable positioning of the sources. In this case only the neutron shielding is used.

Figure 5.9.: Experimental setup with neutron shielding for the measurements 2023.

6. Data preparation and analysis

This chapter will focus on the measurements with the scintillation detectors to study the decay spectrum of the radioactive sources. These results are further utilized to get a deeper understanding of the detectors functionality regarding the ADC-channel energy dependency, which is expected to line up in a linear coherence. Therefore varying measurements with the utilization of the sources Na22, Cs137 and Co60 are foreseen. In preparation, measurement as well as analysis preconditions have to be identified and optimised, such as a cable analysis, positioning of the source, threshold choice or the interpretation of the characteristics of the charge spectrum.
Figure 6.1 shows an example of a charge spectrum of the high gain uDAQ channel of a histogram measurement. The first small peak, around ADC channel 200, is namely the pedestal. It is a resultant of the CPU trigger and is used to evaluate the baseline for the measurements. The pedestal is followed by a small gap. This gap appears, because the trigger threshold is fixed above the baseline. Around ADC channel 1600, the charge spectrum shows a peak, which can be identified as the MIP peak and marks the ADC channel, where a minimum ionized particles passes. The energy loss spectrum of this particle is expected to follow a Landau distribution, with the peak representing the most probable value of the energy loss. This can be approximated through a Gaussian distribution, which was verified in [5] and has been utilised in figure 6.1. This spectrum was taken from a measurement performed at the prototype station, situated at the South Pole. Low temperatures (approximately -50°C) and barely no background noise due to snow layers on the surface, provide ideal conditions for a clearly distinguishable MIP peak. While calibrating the detectors at KIT, these preconditions diminish. The high temperatures (approximately 10°C-30°C) rest in a small gain, whereas, the natural radioactive background and surroundings result in a less defined peak, at lower ADC channels. This can be seen in figure 6.2. However, various configurations can be adjusted to measure and analyse the histograms in the best possible way.

6.1. Preparation

6.1.1. Cable analysis

Before the radioactive source measurements, a set of cables was tested and analyzed to prove their reliability as well as the requirements of the measurements setup. Figure 6.3 shows a multiplot of the 23 cable histogram measurements and display a coherence without significant deviations. The minor shift of a few ADCs is expected due to the environmental fluctuations during the tests. Moreover the fitting of the MIP peak, which can be found at approximately 1000 ADC, proves their alignment. The utilised fit procedure will be

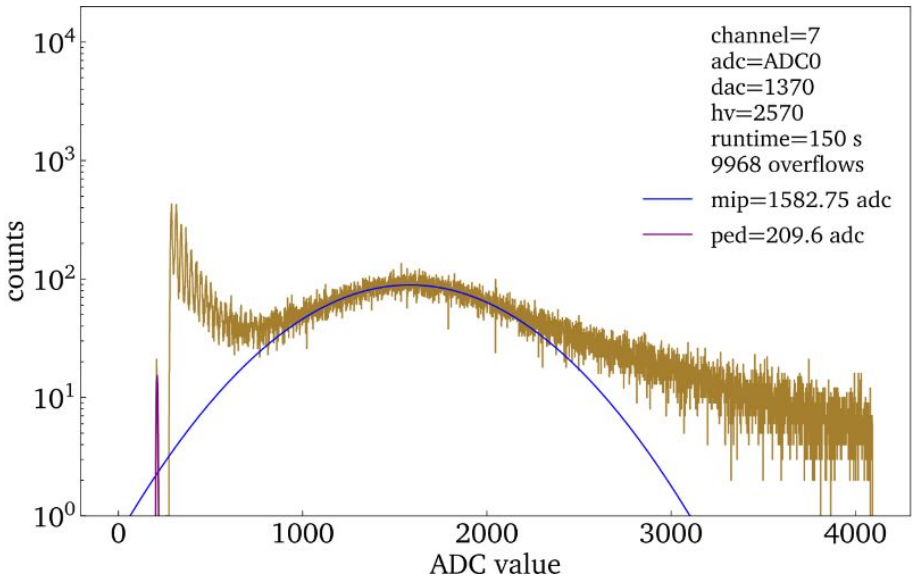

Figure 6.1.: Histogram of a MIP measurement with the prototype of the SAE at the South Pole [5].

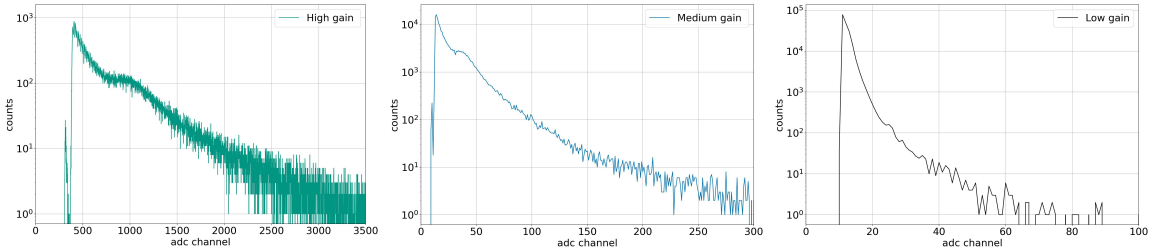

Figure 6.2.: Histogram of an example MIP measurement at KIT. On the left hand side the highest gain is illustrated, the medium gain in the middle and the low gain on the left hand side, where the relevant part of the plot is zoomed in. The peaks get less visible as the gain decreases, because the resolution for lower gains is limited.

discussed in the following sections. The weighted mean of the MIP position and their standard deviation amounts to

$$MIP_{Position} = (959.2 \pm 7.6)\ \text{ADC}-\text{channel}. \tag{6.1}$$

The entirety of the fitted values can be abstracted from the appendix A.1.
The periodic peaks, which can be seen in the following histograms are interpreted as a common mode noise due to the length of the cables and are further analyzed in section 6.2.

6.1.2. Analysis of the radioactive source positions

As earlier mentioned, the structure of the two measurement series differs mostly in the placement of the source. The only variation takes place in the vertical axis regarding the

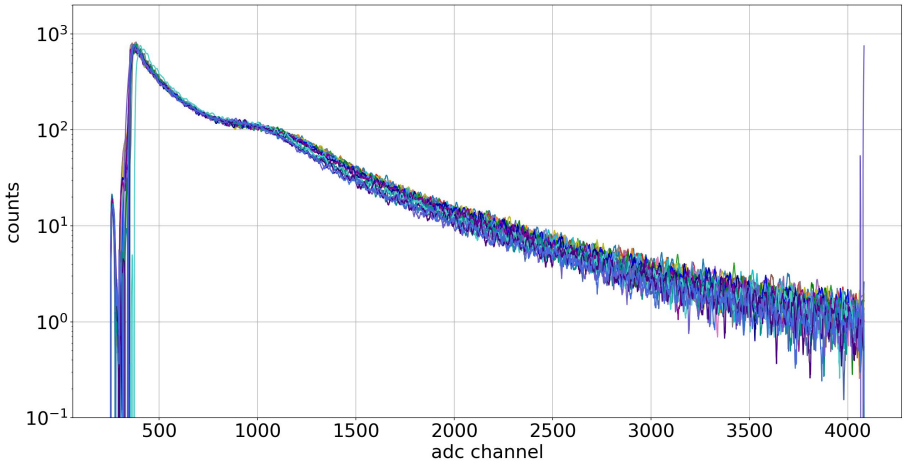

Figure 6.3.: Multiplot of the histograms of a measurement series with 23 cables of 70 m each, tested on the same panel.

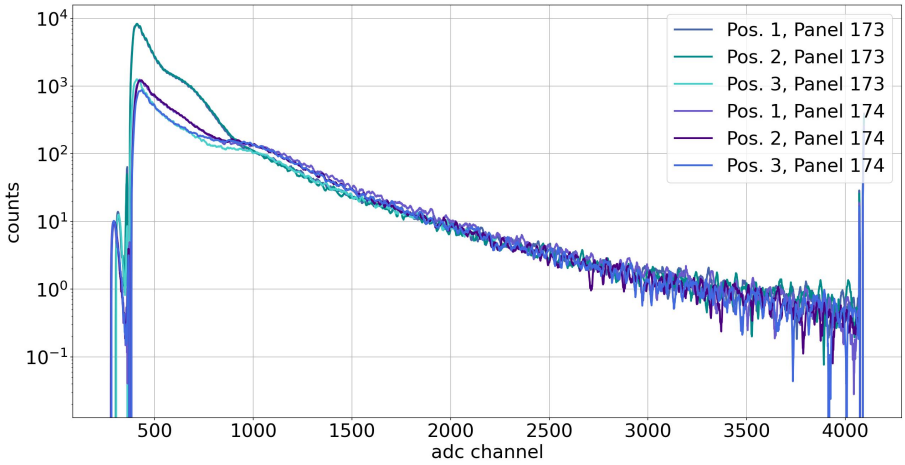

Figure 6.4.: All measurements of sodium for both panels during a 5 minute measurement series performed with a DAC1400 in varying positions.

proximity to the certain panel.
The measurement taken in 2022 has a horizontal variation, where position 1 and position 2 are on different spots on the panel and position 3 is placed in front of the panel. In figure 6.4 the entirety of the measurements from 2022 for both panels and all positions is illustrated. The higher intensity as well as the more distinguished peak, which is identified as MIP peak occur only in the measurements of panel 1 and in position 1 and 2. Position 3 shows few reaction to the sodium source because of it's shielding by the lead layer as well as the distance to the scintillation area as it is in front of the panels. The comparison of position 1 and 2 confirms, that they display the same charge deposit and therefore validates the uniformity of the panel. Thus for the following measurements, performed in early 2023, the position in the middle of the panel was chosen, having no variation in the horizontal dimension, after ascertain the consistency of the panel.

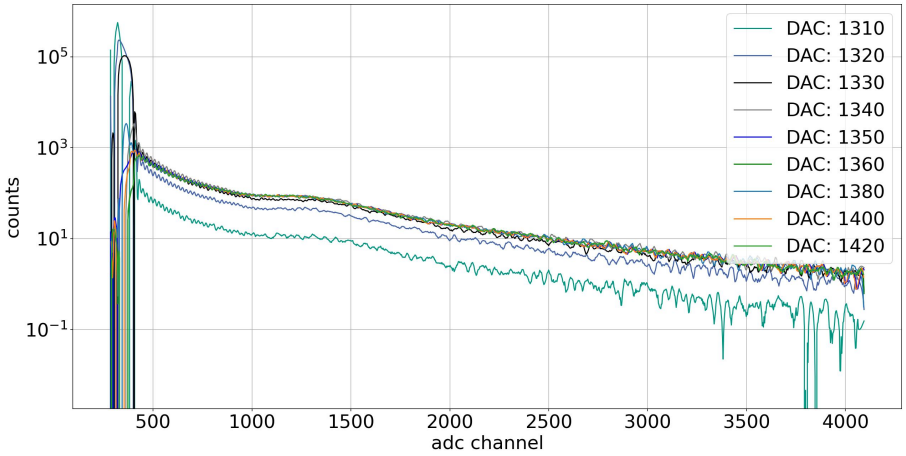

Figure 6.5.: The charge histograms for the different thresholds measured by panel 1, without a source and for a duration of 5 minutes. The variable from 1310 to 1420 was chosen because it covers the region for dark count peak from the SiPM.

6.1.3. Threshold choice

Another parameter choice which would influence the observed charge spectrum with the scintillators is the *threshold*. The threshold determines the value above which the signal is recorded. To find a reasonable value that allows the measurement to contain as much information as possible, several measurements with different thresholds were performed beforehand. In the following the influence of the varying thresholds is illustrated. Figure 6.5 shows the histogram outputs for various thresholds measured by panel 1, the one with the shielding. The measurement was also performed for panel 2, which is added in appendix A.2. The observed sharp increase implies that the threshold trigger coincides with the baseline and later the dark counts. This saturates the electronics and therefore the MIP peak as well as other radioactive source features are missed. Based on this analysis, to avoid triggering on the noise and furthermore confirm the recording of the actual spectrum, the threshold was set at DAC1360 for the measurements in 2023.

6.1.4. Panel absorption

To show that the counts occurring in the detector are additionally influenced by the absorption from another detector, along with neutron and gamma shielding an additional measurement with switched panels was performed. In the first measurement series, panel 1 lays on top of panel 2 and between the shielding as previously explained in figure 5.8. Afterwards the two panels were switched and panel 2 was put on top. Hence, panel 1 is additionally shielded by panel 2 and therefore shows less intensity which can be seen in figure 6.6.

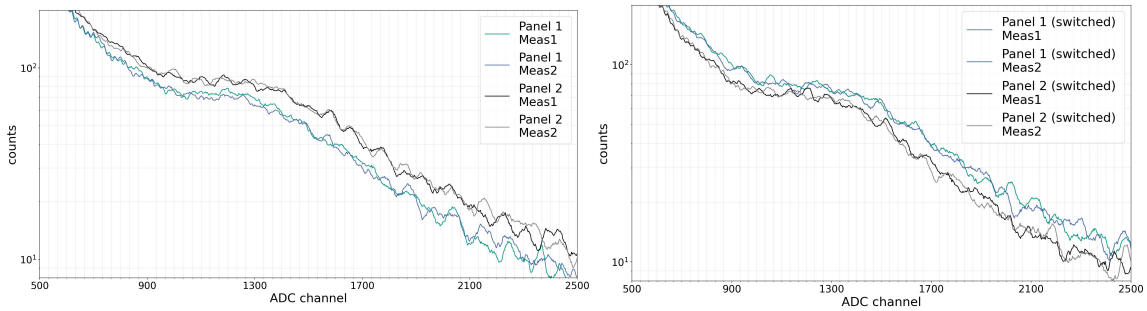

Figure 6.6.: Histogram of a five minute measurement series without any source, in the primary position on the left hand side and the switched position on the right.

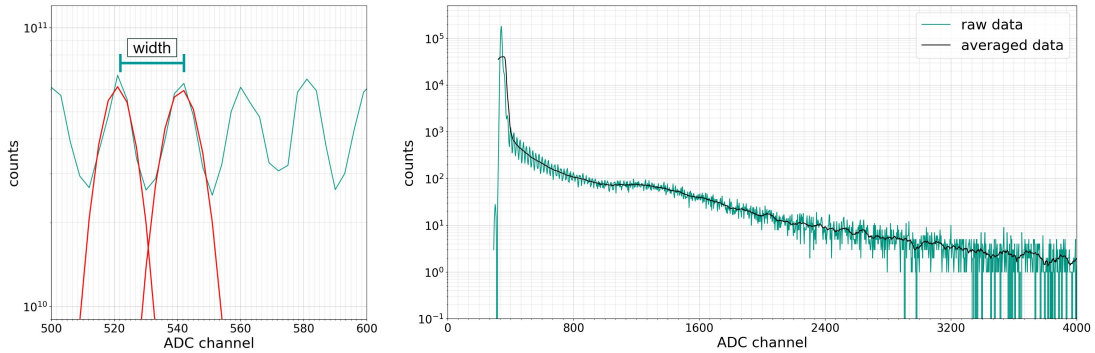

Figure 6.7.: The comparison of the raw data set of a measurement without source and the one by the averaging smoothed data. The x-axis as well as the y-axis show a certain section to deduce the averaging window.

6.2. Data preparation

The visible peaks seen in the measurements are identified either as the MIP peak or as one of the Compton edges from the sources trough a validate fit function and used for further analysis. In order to be able to distinguish these features from noise, a smoothing algorithm is applied on the data. This smoothing process is nearly the same for the MIP peak and the radioactive source characteristics, namely the Compton edges.

MIP peak

The raw data is smoothed through a sliding average algorithm over an ADC range which corresponds to the width of the histograms periodic peaks. These peaks are expected to be a resultant of the common mode noise due to the long (70 m) cables used. For the objective of this thesis, these periodic peaks act as a noise source to the measurements. Hence, the smoothing is performed. Figure 6.7 shows an enlarged segment of one charge histogram with the estimation of the variations width as well as the raw and by this value averaged data.

Compton edges

To clearly distinguish the characteristic shape of the sources' charge spectrum a *difference spectrum* between a measurement with a source and one without is calculated. Thus the noise is filtered and the source characteristics more distinct. Because a few measurement series contain two measurements, the average of both measurements is taken. Furthermore also a sliding average is utilised as explained before for the MIP peak.

6.3. Fit functions

The analysis relies mainly on the estimation of the visible peaks due to the radioactive sources and the MIP peak. For this estimation, it is vital to use a fit function that best describes the spectrum. The MIP peaks are estimated by a fit with a Gaussian and further with a Landau distribution. For the Compton edge peaks two functions were tested: A modified Gaussian function that is emerged from a Heaviside distribution and a Gaussian distribution.

6.3.1. Fitting the MIP peak: Gaussian and Landau

In contrast to the high energetic photons, which are emitted by the radioactive sources, the MIPs, that are expected, are charged particles, in this case muons. They interact directly with the atoms and molecules of the scintillator and deposit a fraction of their energy whilst tearing out a few of the shell electrons (delta rays) [43]. This interaction results in a charge spectrum that has a characteristic peak followed by a gradual decay like tail. This kind of spectrum is best described by a Landau distribution. As a prefitting a Gaussian distribution was used [5].

The MIP peak can be fitted with the probability density function

$$G(E) = a * \exp\left(-\frac{1}{2} * \frac{(x-\mu)^2}{\sigma^2}\right) \tag{6.2}$$

where the amplitude a represents the height of the curve's peak, the mean μ the position of the center of the peak and the standard deviation σ controls the with of the Gaussian 'bell'.

Another, more precise, fit function might be the Landau distribution, whereas it takes also the lower tail after the MIP peak into account. Therefore the MIP peaks are fitted through a Gaussian distribution which estimates the free parameters used in the Landau distribution following the function

$$L(E) = \frac{a\sigma}{\sqrt{2\pi}} \exp\left(-\frac{(x + \exp(-x))}{2}\right). \tag{6.3}$$

Figure 6.8 shows an example of a Landau fit whose parameters are assigned from the Gaussian fit. In the following all MIP peaks are fitted by a Landau distribution with parameters confirmed by the Gaussian fit.

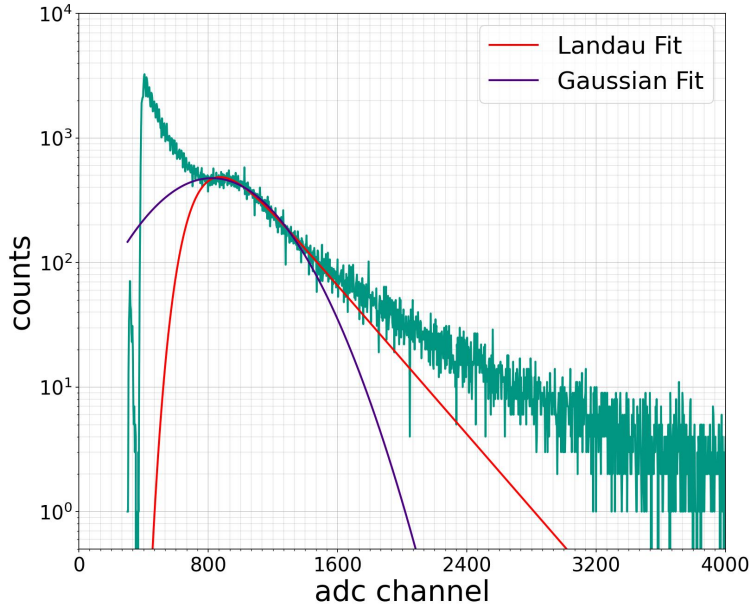

Figure 6.8.: The Gaussian fit as well as the by the Gaussian implied Landau fit displayed in one histogram.

6.3.2. Fitting the Compton edges: Modified Gaussian and Gaussian

The main idea leading to the function used to fit a Compton edge relays on the fact that a portion of the the response could be modeled by a Heaviside step function (HSF) [52]

$$H(E) = \begin{cases} 1, & E \leq E_c \\ 0, & E > E_c \end{cases} \tag{6.4}$$

while the peak in its latter part can be identified as a Gaussian distribution

$$G(E) = \frac{1}{\sqrt{2\pi}\sigma} * \exp\left(-\frac{1}{2} * \frac{E^2}{\sigma^2}\right). \tag{6.5}$$

The *real* response function $R(E)$ that can be utilized for the fitting emerges from convolution of the *ideal* response function $r(E)$ into the Gaussian distribution. Where the *ideal* Compton edge could be described by

$$r(E) = \begin{cases} (aE^2 + bE + c), & E \leq E_c \\ 0, & E > E_c \end{cases} \tag{6.6}$$

with the maximal value E_c shown in figure 6.9.

Including the convolution of the *ideal* Compton edge in the corresponding Gaussian distribution (7.3) the *real* Compton edge results in

$$R(E) = \alpha_1 * \mathrm{erfc}\left(\frac{E - E_c}{\sqrt{2}\sigma}\right) + \beta_1 * \exp\left(-\frac{(E - E_c)^2}{2\sigma^2}\right), \tag{6.7}$$

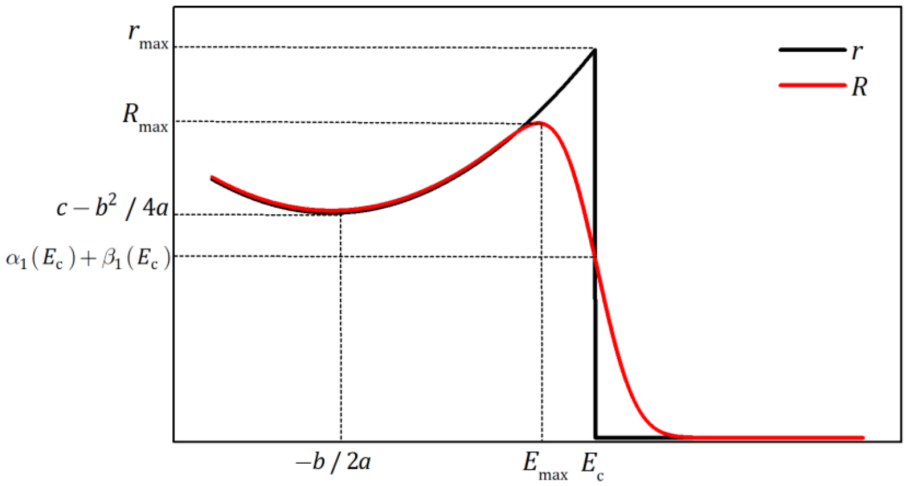

Figure 6.9.: Modified Gaussian found through an adjustment of the Heaviside step function [52].

with the complementary error function

$$\operatorname{erfc}(E) = 1 - \frac{2}{\sqrt{\pi}} \int_0^E \exp\left(-x^2\right) dx \tag{6.8}$$

and

$$\alpha_1(E) \equiv \frac{1}{2}\Big[a(E^2 + \sigma^2) + bE + c\Big], \tag{6.9}$$

$$\beta_1(E) \equiv \frac{-\sigma}{\sqrt{2\pi}} a(E + E_c) + b. \tag{6.10}$$

With the arithmetic expression we found in equation (7.5) the Compton edges can be fit and the value for the corresponding ADC channels be found [52]. The value E_c corresponds to the energy value of the Compton edge E_{max}.

Although the modified Gaussian seems to be a valuable fit function for the Compton edges, it heavily relies on the prominence of the individual features. However, due to the environmental conditions of the utilised setup and the properties of the detector, as well as the mutual overlap of the Compton edges and the MIP peak, the shape of the edges are not as clearly distinguishable as in figure 6.9, which is illustrated in figure 6.11. Figure 6.10 shows a measured histogram with radioactive source fit twice, with the modified Gaussian, while slightly varying the fitting range. The obtained E_c from these flatter significantly indicates that the fit parameters and therefore their functions seems to be very sensitive and therefore not reliable.

Nevertheless the observed part of the Compton edge can be approximated through a Gaussian distribution. To include the effect, that both Compton edges lay close to each other, a Gaussian sum distribution was utilised to fit the two characteristics combined:

$$G_{sum}(E) = a_1 * \exp\left(-\frac{1}{2} * \frac{(x - \mu_1)^2}{\sigma_1^2}\right) + a_2 * \exp\left(-\frac{1}{2} * \frac{(x - \mu_2)^2}{\sigma_2^2}\right) \tag{6.11}$$

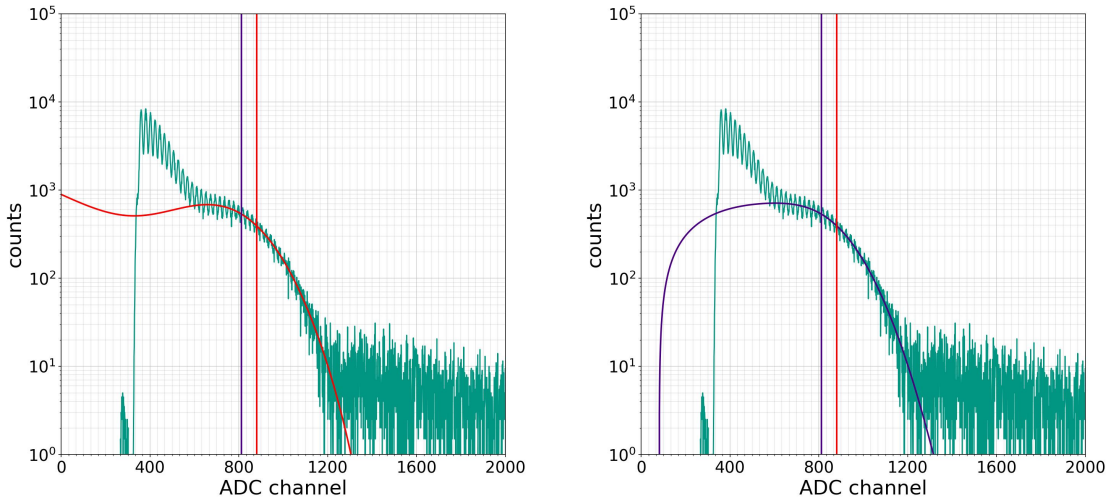

Figure 6.10.: Example of the sensitiveness of the modified Gaussian with the shifted E_c for varying parameters.

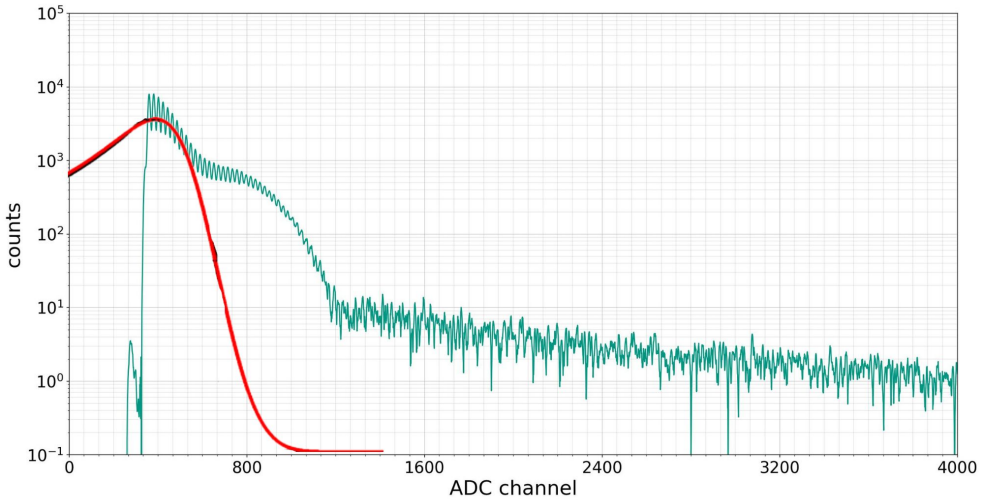

Figure 6.11.: Gaussian part of the Compton edge compared with the modified Gaussian fit presented in figure 6.9.

The location of the Compton edge can be assumed through the comparison to the value of the Gaussian mean count-rate. It is described by the percent the count-rate deviates from its maximum value at the mean. This percentage is widely discussed and the nuclear physics communities suggestions range from 66% [53] up to 89% [54]. The reason for these variances has its root in the various effective resolution of the used detection systems. In the case of this thesis and the work with plastic scintillation detectors 70% is expected to serve best [55, 43], but for completeness, the entire percentage band width is investigated in this work.

Goodness of fit

To prove the goodness of the used fitting methods a chi-squared test is used. The X^2 values of a fit are calculated via

$$X^2 = \sum \frac{(O_i - E_i)^2}{E_i}. \tag{6.12}$$

The variable O_i describes the observed values, the values which are the base of the fit, and E_i represents the expected values, the values of the fit. The X^2 values divided by the number of degrees of freedom (ndf) gives the goodness of a fit and can be further compared throughout the fitting methods.

At this point resonable preconditions are found, confirming the neccessity of a shielding as well as the uniformity of the panels and cables. Furthermore the data proceedings were analyzed and a by the chi-square test proved fit method was ascertained. With these results the fits including all measurement series is possible and presented in chapter 7.

7. Calculation of the ADC-Energy-Relation

7.1. Fitting results

In the following sections the fitting results are discussed, once for the early measurements in 2022 and once for the ones in 2023. For each measurement three characteristics are determined: *the pedestal*, *the Compton edges* and the *MIP*. The results of the fitted positions differ by the most influential environmental condition, the varying temperature. The only exception is the position of the pedestal, which is independent of the temperature.

7.1.1. Data set 2022

Without source

The measurement without any source serves mainly as a reference. Overall four measurements with each panel were performed with changing threshold and duration. In figure 7.1 the fits are illustrated for both panels for one measurement. The MIP peak is fit with the Landau distribution relying on the pre-estimated parameters by the Gaussian distribution as described in section 6.3.1. In the table 7.1 the summary of all measurements of the first series is shown. Figure 7.1 displays the fit plot of the MIP peak as well as the pedestal. In the further analysis the value of the pedestal is taken from the measurements without any source providing ideal conditions.

	Threshold	Duration		Panel 1	Panel 2
Pedestal	DAC 1360	5min	Measurement 1	-	-
	DAC 1400	5min	Measurement 1	316.0 ± 9.9	295.2 ± 8.1
		5min	Measurement 2	317.5 ±7.8	296.4 ± 1.9
		20min	Measurement 1	317.5 ± 0.3	296.3 ± 0.3
MIP	DAC 1350	5min	Measurement 1	907.1 ± 10.0	897.9 ± 14.7
	DAC 1400	5min	Measurement 1	910.6 ± 7.2	902.4 ± 14.4
		5min	Measurement 2	902.2 ±11.6	903.7 ± 14.9
		20min	Measurement 1	895.2 ± 3.7	895.0 ± 5.9

Table 7.1.: Fitting results of all measurements without source and their resembling standard deviation error.

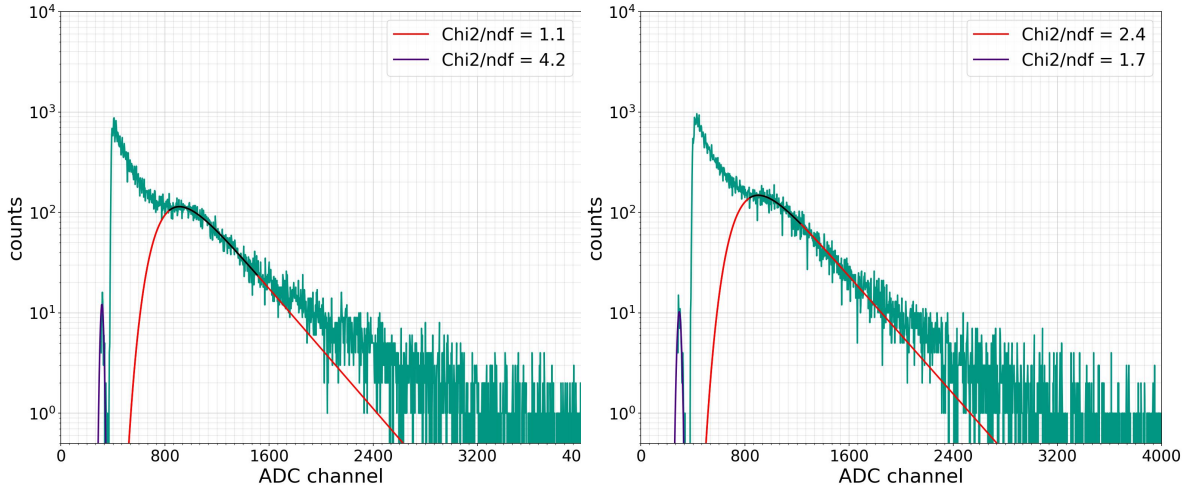

Figure 7.1.: Fitting of the MIP peak for a 5 minute measurement without a source with the threshold DAC1400 for measured data from panel 1 shown on the left and panel 2 on the right hand side.

Americum-Beryllium

Considering the histogram of the measurement with the neutron source, figure 7.2, it can be seen, that the active source emits over the whole energy range and overlays the characteristic position of the MIP peak. Figure 7.2 demonstrates, that no clear peak/edge is recognizable. AmBe irradiates the entire range and is therefore not usable for the energy calibration. However, it can be seen, that the emission is located in the range after the valley and is expected with the highest values between 0.5 MeV and 4.2 MeV [56], which confirms the charge histogram measuring the correct energy range.

Sodium-22 (Na22)

The measurement series with the source Na22 consists of six measurements. In each measurement the data of both panels is collected and the threshold, the position and the duration is varied. For the presented plots in figure 7.3 the Na22 source was placed in position 1 with the threshold DAC 1400 and a duration of 5 minutes. In figure 7.3 the fitting of the pedestal is shown, as well as the one of the Compton edges, fit with the Gaussian sum distribution 6.11. The plot is a difference plot between a measurement with and without Na22 source and averaged by a the width of the cable uncertainties. The results regarding position 2 as well as a longer measurement are added in the appendix A.4.2. The measurements in 2022 were performed without a shielding on panel 2. That is why the background is very high and beneath the edges, also some pedestal values were indistinguishable. In these cases, the pedestal is too overlaid by the noise and too spread out, because of the saturation of the electronics and therefore left out to avoid errors. All fits, that are not taken into account, are displayed with brackets. Moreover, Resembling to the measurement of AmBe sodium displays a high decay range in the second Compton edge and overlays the MIP peak. Therefore a fitting of the MIP isn't possible either.

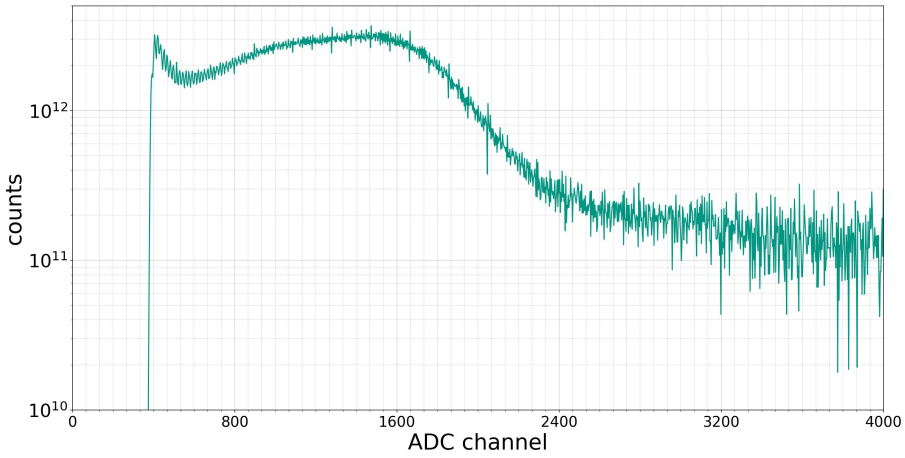

Figure 7.2.: The histogram of the source AmBe placed in position 1, with the threshold DAC 1400 and a duration of 20 minutes measured by panel 1.

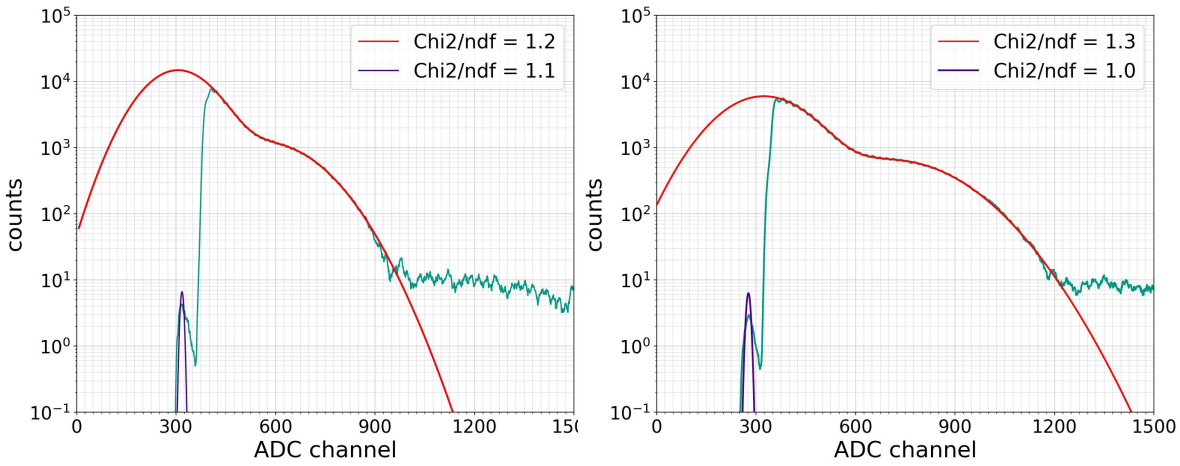

Figure 7.3.: Combined Gaussian fit of both sodium Compton edges. Left: measured by the panel 1; right: measured by the unshielded panel 2.

		Position	Duration	Panel 1	Panel 2
Na22	Pedestal	Position 1	5min	(320.6 ± 2.4)	(300.3 ± 2.0)
			30min	(316.1 ± 1.0)	(299.2 ± 2.7)
		Position 2	5min	-	-
		Position 3	5min	(319.9 ± 2.0)	-
	First edge	Position 1	5min	384.1 ± 11.1	-
			30min	380.0 ± 6.8	-
		Position 2	5min	384.6 ± 14.7	-
		Position 3	5min	392.3 ± 29.9	-
	Second edge	Position 1	5min	663.7 ± 7.4	-
			30min	662.3 ± 4.0	651.3 ± 8.7
		Position 2	5min	673.6 ± 7.4	-
		Position 3	5min	-	-

Table 7.2.: Fitting results for all measurements with sodium and their resembling standard deviation error. The threshold was maintained at DAC 1400 for all measurements. The values in the brackets aren't considered because of the sources' influence on the pedestal as earlier explained.

In the spreadsheet 7.2 the fitting results of all measurements are presented and later on used for the further evaluation. As already mentioned, the energy of the Compton edge will resemble to 70% of the per Gaussian/Landau estimated parameters, as it is utilized in the following result tables. The Compton edges are hereafter always considered as 70% of the Gaussian mean count-rate, as explained in section 6.3.2. Panel 2 in the long measurement in position 1, position 2 and position 3 weren't considered, because the edges weren't able to fit, respectively the panel didn't record anything due to the shielding.

Cesium-137 (Cs137)

For Cs137 the same configuration as before is used. The entirety of the measurements with cesium comprises twelve measurements, six measurements per panel, with varying threshold, positions and duration. Figure 7.4 shows the plot of the fit Compton edge caused by the cesium source as well as the fit of the pedestal, both realised through a difference and averaged plot. Figure 7.5 illustrates the fitting of the MIP peak for both panels. The table 7.3 illustrates the overview of all results from the measurements with the cesium source. Equally to the measurement with sodium, panel 2 is missing a shielding in this measurement series, which increases the uncertainties on the fits and lowers the goodness of them.

7.1.2. Data set 2023

The threshold of the DAC 1360 was chosen as the optimal threshold like it's illustrated in chapter 6.1.3. Moreover all measurement series contain two measurements, which are

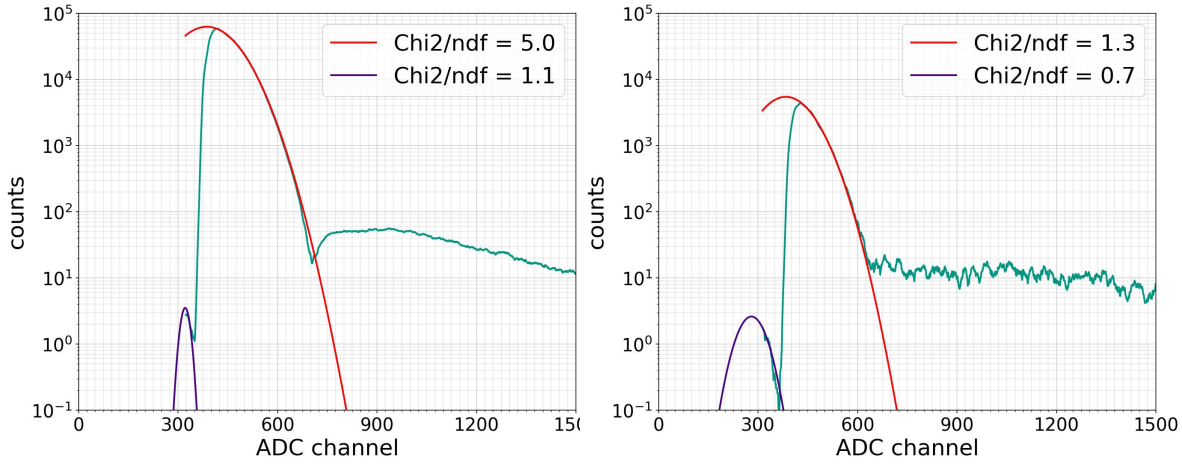

Figure 7.4.: Gaussian fit of the pedestal from the measurement with cesium. Left: measured by the panel 1; right: measured by the unshielded panel 2.

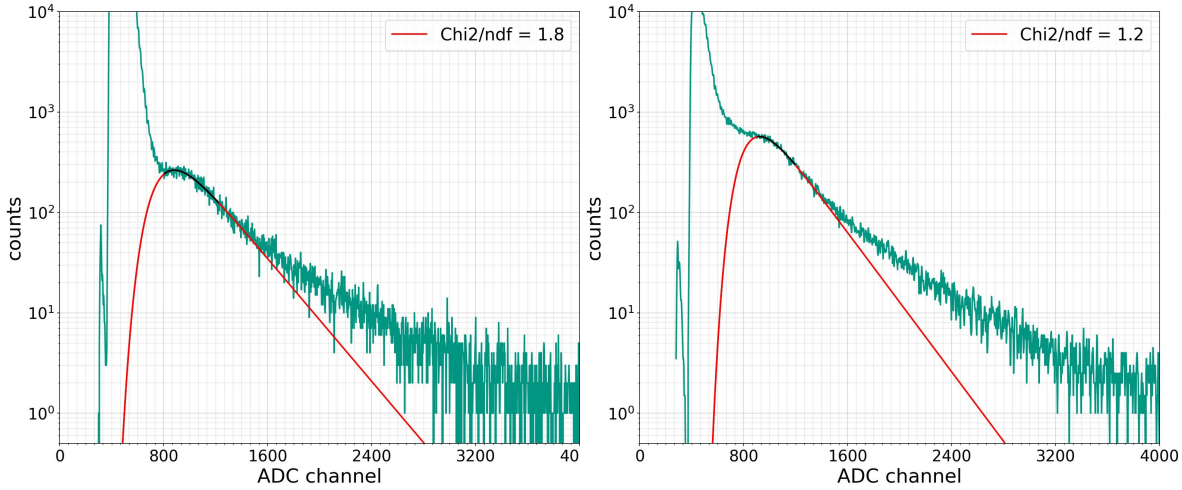

Figure 7.5.: Gaussian MIP peak fit of the measurement with cesium. Left: measured by the panel 1; right: measured by the unshielded panel 2.

		Position	Duration	Panel 1	Panel 2
Cs137	Pedestal	Position 1	5min	(321.6± 2.3)	(315.6 ± 12.2)
			30min	(309.3 ± 14.3)	-
		Position 2	5min	(320.5 ± 1.9)	-
	First edge	Position 1	5min	455.5 ± 0.6	444.3 ± 1.8
			30min	460.7 ± 0.5	445.8 ± 1.7
		Position 2	5min	459.7 ± 0.7	441.3 ± 5.1
	MIP	Position 1	5min	907.3 ± 22.5	908.8 ± 12.3
			30min	907.1 ± 11.3	912.0 ± 9.5
		Position 2	5min	906.9 ±12.9	897.5 ± 13.3

Table 7.3.: Fitting results of all relevant measurements with cesium and their resembling standard deviation error, performed with the threshold DAC 1400. The values in the brackets (the pedestal) weren't considered further on.

combined for the fitting by taking a weighted mean for the further analysis through the difference plots.

Without source

Likewise to the preciously measured series, a reference measurement without any source was taken. The series comprises two measurements of both panels with a duration of five minutes, a threshold DAC 1360 and another two measurements with the same conditions but switched panels (panel 2 on top and panel 1 on the bottom). In the following the MIP peak is fitted first by a Gaussian distribution and the estimated parameters passed on to a Landau fit. Both histograms were averaged. Figure 7.6 illustrates the fitting of the MIP for the first two measurements for both panels and the table 7.4 below shows their results. The table 7.5 shows the measurements with switched panels. In the appendix A.4.1 the additional plots are shown.

Sodium-22 (Na22)

For the measurements with the active sources, they could either be placed above both panels (position 1) or in between the panels, with panel 1 on top (position 2). One can observe a slight difference in the measured peaks in both position. In position 2 the shape is a bit more distinct in both panels and hence easier to fit because the shielding from the panel itself is avoided. Therefore position 2 is illustrated in the following. Position 1 can be found in the appendix A.4.2. Figure 7.7 shows the fitting of the first and second Compton edge. In the table 7.6 the results are collected.

Cobalt60

A.4.3 The measurements with the source Co60 is performed with the configurations with the only exception of an additionally measurement in position 2 over 20 minutes.

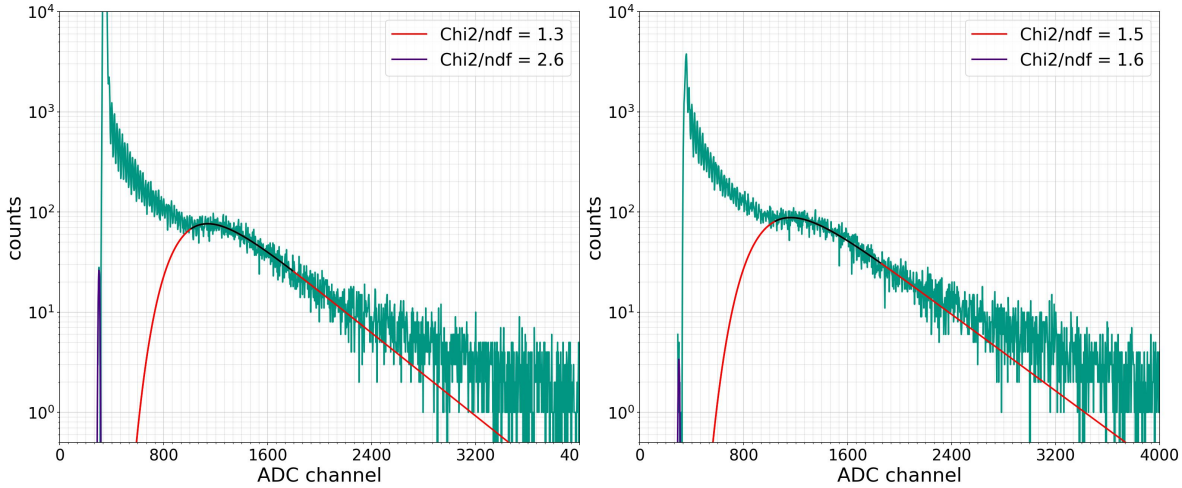

Figure 7.6.: Gaussian MIP fit without a source.

		Duration	Panel 1	Panel 2
Pedestal	5min	Measurement 1	302.4 ± 0.1	301.4 ±2.5
	5min	Measurement 2	301.8 ± 0.7	294.8 ± 6.3
MIP	5min	Measurement 1	1156.7 ± 11.6	1162.2 ± 13.4
	5min	Measurement 2	1160.3 ± 16.6	1166.2 ± 11.1

Table 7.4.: Fitting results of all the new measurements without source and a threshold of DAC 1350 as well as their resembling standard deviation error.

		Duration	Panel 1	Panel 2
Pedestal	5min	Measurement 1	301.1 ± 0.2	-
	5min	Measurement 2	302.2 ± 0.2	-
MIP	5min	Measurement 1	1153.8 ± 18.6	1160.4 ± 24.2
	5min	Measurement 2	1164.6 ± 19.4	1170.0 ± 18.4

Table 7.5.: Fitting results of all the new measurements without source with the switched position of the both panels and a threshold of DAC 1350 as well as their resembling standard deviation error.

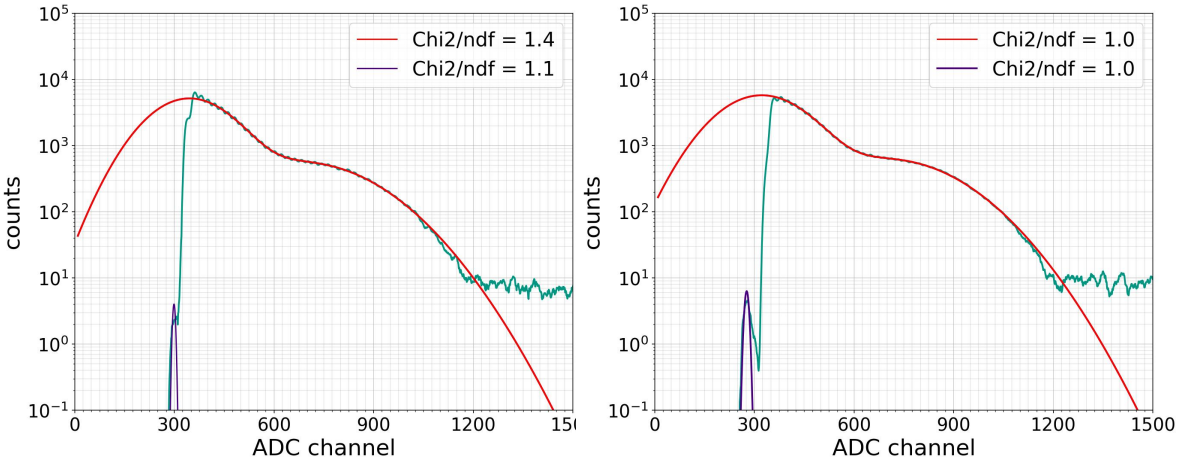

Figure 7.7.: Gaussian sum fit of the Na22 Compton edges in position 2.

		Position	Duration	Panel 1	Panel 2
Na22	Pedestal	Position 1	5min	(318.4 ± 1.1)	(279.2 ±0.7)
		Position 2	5min	(320.4 ± 0.5)	(277.8 ±0.8)
	First edge	Position 1	5min	431.1 ± 8.0	442.2 ± 1.9
		Position 2	5min	440.1 ± 4.4	444.8 ± 5.5
	Second edge	Position 1	5min	796.8± 13.4	828.2 ± 9.8
		Position 2	5min	822.5 ± 9.3	829.1 ±10.8

Table 7.6.: Fitting results of all new measurements of Na22 and their resembling standard deviation error. A measurement series with two measurements for each position, averaged for the Compton edges. The values in the brackets (the pedestal) weren't considered further on.

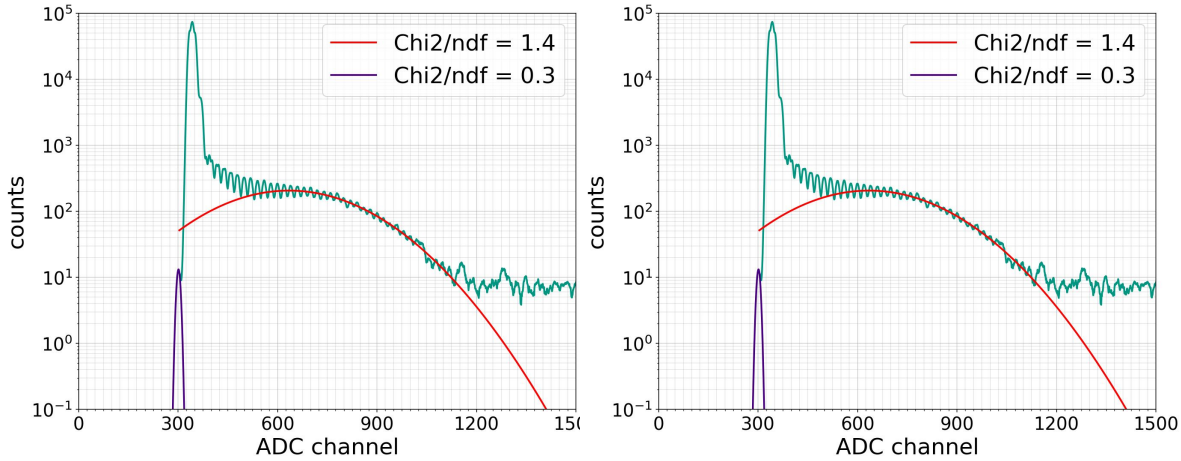

Figure 7.8.: Gaussian Fit of both Compton edges with the Co60 source, DAC1360, 5 minute measurements in position 2.

		Position		Panel 1	Panel 2
Co60	Pedestal	Position 1	Measurement 1	(305.1 ± 0.6)	-
		Position 2	Measurement 1	(301.4 ± 0.3)	(285.9± 1.2)
	First edge	Position 1	Measurement 1	795.8 ± 6.6	812.9 ± 2.9
		Position 2	Measurement 1	801.9 ± 4.5	806.5 ± 3.3
	MIP	Position 1	Measurement 1	1140.9 ± 26.5	1134.5 ± 39.4
			Measurement 2	1138.5 ± 25.4	1140.3 ± 34.9
		Position 2	Measurement 1	1139.6± 28.9	1144.3± 21.0
			Measurement 2	1140.6 ± 30.9	1143.8 ± 28.2

Table 7.7.: Fitting results of all new measurements of Co60 and their resembling standard deviation error. A measurement series with two measurements for each position and 5 min. The values of the pedestal (displayed in brackets) weren't used further on.

All results are displayed in the spreadsheet 7.7 and the corresponding plots with the fits in figure 7.8 for the first peak and in figure 7.9 for the MIP peak. Position 1 can be found in the appendix A.4.3.

7.1.3. Peak identification

Regarding all measurements and their uncertainties they can be utilised to establish a relation with the characteristic Compton edge energies of the source. The deposited energy of the Na22 Compton edge amounts to:

$$Na22_{FirstCompton} = 340\text{keV}\ [57]. \tag{7.1}$$

$$Na22_{SecondCompton} = 1060\text{keV}\ [57]. \tag{7.2}$$

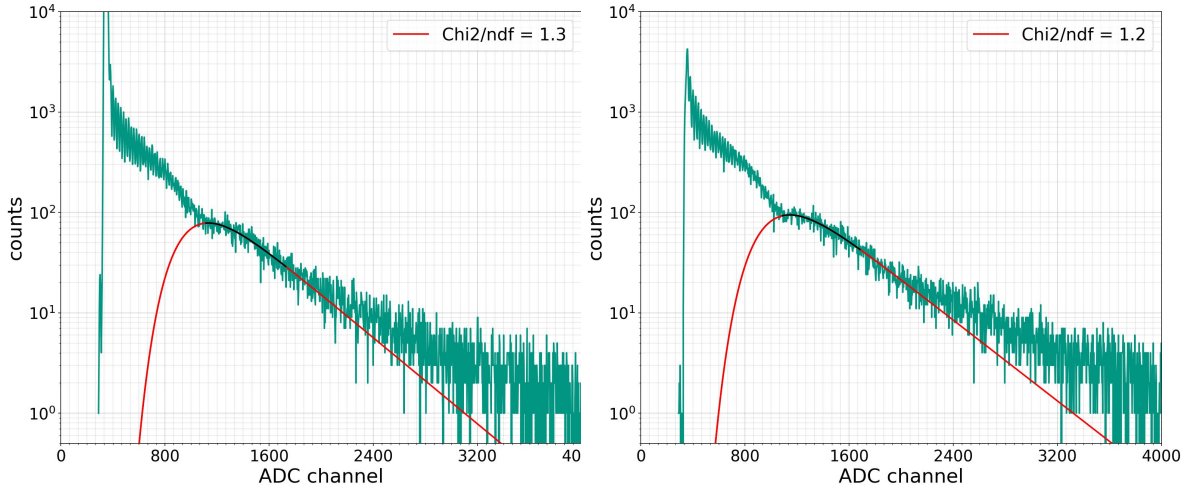

Figure 7.9.: Co60 Gaussian Fit of the MIP averaged and with a DAC1360, 5 minute measurement in position 2 for both panels: panel 1 left and panel 2 right.

The Compton edge for the Cesium photo peak is to be found at:

$$Cs137_{FirstCompton} = 480\text{keV}\ [57]. \tag{7.3}$$

The peak which is visible in the measurement with Cobalt is an overlay of the Compton edges relating to both the photo peaks. Hence the average sums up to:

$$Co60_{FirstCompton} = 1040\text{keV}\ [43]. \tag{7.4}$$

7.1.4. ADC channel assignment

The collection of all measured results build the foundation to the determining part of the calibration. The relation between ADC channel and the energy spectrum follows from the linearity estimated utilising the measured ADC values of the Na22 as well as the Cs137 and Co60 Compton edges and their mapping them to their known energy levels. These calculations are regarded separately for each measurement because of the altered measurement conditions, such as duration, position and panel.

Data set 2022

In the table 7.8 the ADC channel assignments for the peaks of the 2022 measurements are illustrated. The fitted values of the MIP measurement are taken as a weighted mean, because their uncertainties are expected to be lower due to their independence of the varying source position. Moreover, also the pedestal peaks of the measurements without source are taken as a weighted mean.
Figure 7.10 shows the plot of the calculated linearity for the measurements in 2022 and it is getting clear, that the regression slope doesn't differ much within one measurement series. The linear fit includes a series of five measurements, separately fitted, considering the pedestals weighted of the measurements without a source, both Compton edges of

		Peak position (ADC channels)	Expected energy deposit
Cs137	1. Compton edge	455.5 ± 0.6	480 keV
		460.7 ± 0.5	480 keV
		459.7 ± 0.7	480 keV
		444.3 ± 1.8	480 keV
		445.8 ± 1.7	480 keV
		441.3 ± 5.1	480 keV
	MIP	907.4 ± 5.1	1500-2000 keV
Na22	1. Compton edge	384.1 ± 11.1	340 keV
		380.0 ± 6.8	340 keV
		384.6 ± 14.7	340 keV
		392.3 ± 29.9	340 keV
		391.9 ± 16.7	340 keV
	2. Compton edge	663.7 ± 7.4	1060 keV
		662.3 ± 4.0	1060 keV
		673.6 ± 7.4	1060 keV
		651.3 ± 8.7	1060 keV
		648.0 ± 4.8	1060 keV
Without source	Pedestal	306.8 ± 0.2	0 keV
	MIP	898.8 ± 2.6	1500-2000 keV

Table 7.8.: Peak identification of all measurements from 2022.

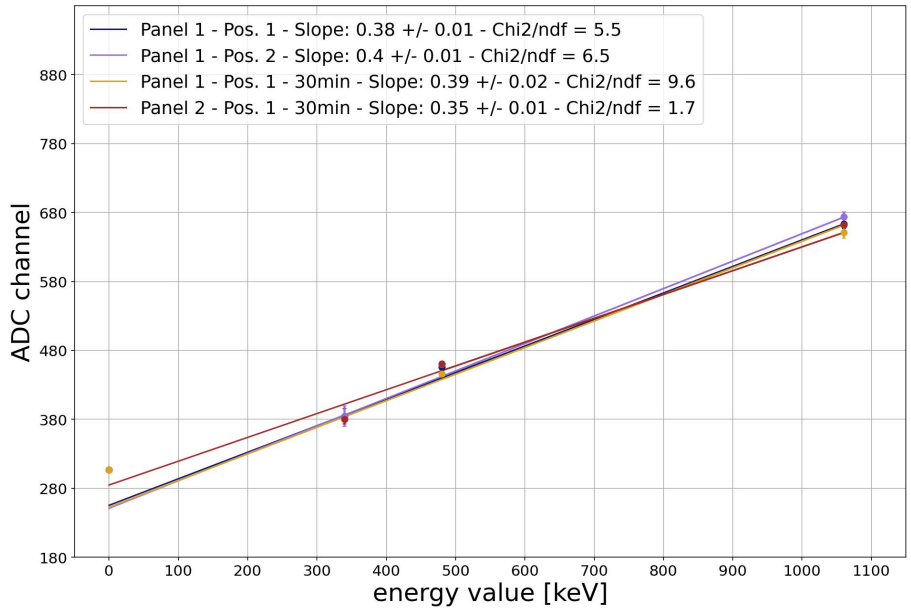

Figure 7.10.: Four linear fits of the Na22 and Cs137 measurements from 2022.

Measurement	Slope	Chi-squared test
Panel 1 - 5 min - Position 1	0.38 ± 0.01	$\frac{Chi^2}{ndf} = 5.5$
Panel 1 - 5 min - Position 2	0.40 ± 0.01	$\frac{Chi^2}{ndf} = 6.5$
Panel 1 - 30min	0.39 ± 0.02	$\frac{Chi^2}{ndf} = 9.6$
Panel 2 - 30min	0.35 ± 0.01	$\frac{Chi^2}{ndf} = 1.7$

Table 7.9.: ADC-energy relation for the measurements of 2022.

Na22 and the Compton edge of Cs137. The Compton edges were interpreted as 70% of the Gaussian mean count-rate as explained in section 6.3.2. Thereby the relation between the ADC channel and the corresponding energy value is gained. It is getting visible that the particular estimated values of the sources display a good linearity. The table 7.9 collects the various slopes defining the ADC-energy correlation and their standard deviation as well as their chi-squared test representing the goodness of the fit. Clearly, the chi-square-test is rather high for some of the linear fits. Especially the measurements with panel 1 in position 1 and position 2 as well as panel 1 in position 1 (30min) display a bad chi-square-test, which is caused mainly by the experimental setup of the measurements. Due to the missing shielding in these measurement series, the background is very high and some peaks indistinguishable. Especially the first Compton edge of Na22 was either missed completely or difficult to fit. The measurement of panel 2 in position 1 displays a better $\frac{Chi^2}{ndf}$, but consists in contrast to the other measurements just of three data points (first Compton edge of Na22 is missing). In the appendix A.5.1 the entire equations of the linear regressions are displayed.

		Peak position (ADC channel)	Expected energy deposit
Co60	1. Compton edge	795.8 ± 6.6	1040 keV
		801.9 ± 4.5	1040 keV
		812.9 ± 2.9	1040 keV
		806.5 ± 3.3	1040 keV
	MIP	1141.0 ± 9.9	1500-2000 keV
Na22	1. Compton edge	442.2 ± 1.9	340 keV
		431.1 ± 8.0	340 keV
		444.8 ± 5.5	340 keV
		440.1 ± 4.4	340 keV
	2. Compton edge	828.2 ± 9.8	1060 keV
		796.8 ± 13.4	1060 keV
		829.1 ±10.8	1060 keV
		822.5 ± 9.3	1060 keV
Without source	Pedestal	302.1 ± 0.1	1500-2000 keV
	MIP	1161.8 ± 5.3	1500-2000 keV

Table 7.10.: Peak identification of all measurements from 2023.

Measurement	Slope	Chi-squared test
Panel 1 - 5 min - Position 1	0.51 ± 0.01	$\frac{Chi^2}{ndf} = 3.7$
Panel 1 - 5 min - Position 2	0.52 ± 0.01	$\frac{Chi^2}{ndf} = 3.0$
Panel 2 - 5 min - Position 1	0.53 ± 0.01	$\frac{Chi^2}{ndf} = 2.7$
Panel 2 - 5min - Position 2	0.53 ± 0.01	$\frac{Chi^2}{ndf} = 2.5$

Table 7.11.: ADC-energy relation for the measurements of 2023.

Data set 2023

In the table 7.10 the peak positions for the measurements from 2023 are illustrated, again with the MIP and the pedestal implemented by a weighted mean. With the same calculating procedure the relation between the ADC channel and the energy value for the second measurements is estimated. In figure 7.11 the fits of the Na22 and Co60 characteristics are put into a linearity and delivers the relations between the ADC channel and the energy value for each measurement. In this case four measurements built the linear regressions. Likewise fitted with both pedestals and the Compton edges of both sources. The Compton edges were interpreted as 70% of the Gaussian mean count-rate as explained in section 6.3.1. The table 7.11 shows this coherence with their standard deviation as well as the chi-squared tests, which show in average a better alignment than in the previous measurements. The entire equations of the linear regression can be found in the appendix A.5.2.

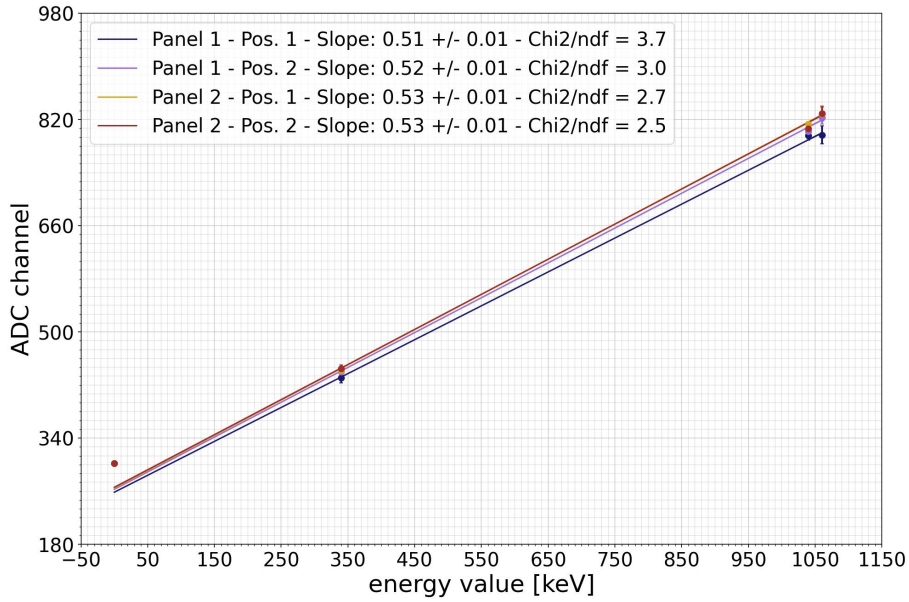

Figure 7.11.: Four linear fits of the Na22 and Co60 measurements from 2023.

Linearity confirmation

According to the estimated ADC-energy linearity the energy range of the MIP peak is examined. Therefore the weighted means of the measured ADC channel is spread over the energy band of $E_{MIP} = 1500$ keV $-$ 2000 keV and compared with the calculated linear ADC-energy plots for illustration. Figure 7.12 presents the collected results of the calibration with the linear fits of the various measurements building a range corresponding to the assumed values of the MIP peak. Furthermore these fits consider the lowest assumed Compton edge percentage of 66% as well as the highest assumed percentage of 80%. Both measurement series are illustrated and differ mostly because of the varying temperature, which influences the ADC channel recording due to the change in the SiPM gain. The range where the MIP is expected align with the calculated band of the linear regressions. The following table 7.12 compiles the calculations for the energy level of the MIP peaks and confirms their energy which was assumed in the range of $E_{MIP} = 1500$ keV $-$ 2000 keV. Moreover the MIP energy range can be bounded through the 70 % interpretation of the Compton edges. Hence the MIPs energy ranges between $E_{MIP} = 1631$ keV and 1803 keV.

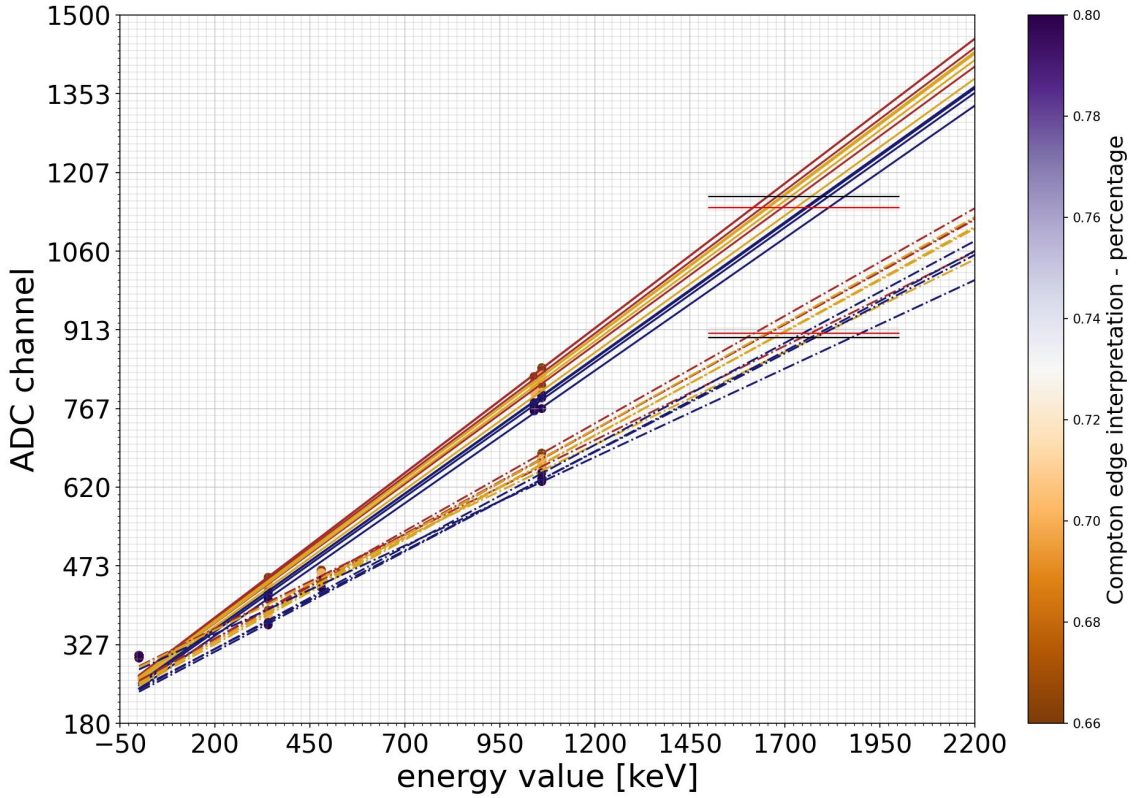

Figure 7.12.: Linear fits of both measurements series with variation in the assumption of the Compton edge positions combined with the MIP peak measurements. The dotted lines present the data set from 2022 and the solid lines the data set from 2023.

		2022		2023	
Calculation method		Without source	Cs137	Without source	Co60
	66%	1636.7 keV	1658.7 keV	1732.7 keV	1692.6 keV
Panel1-1	70%	1671.8 keV	1694.1 keV	1769.2 keV	1728.5 keV
	80 %	1779.5 keV	1802.9 keV	1856.6 keV	1814.5 keV
	66%	1598.4 keV	1619.9 keV	1678.8 keV	1639.8 keV
Panel1-2	70%	1631.3 keV	1653.1 keV	1714.5 keV	1674.9 keV
	80 %	1725.6 keV	1748.2 keV	1814.7 keV	1773.3 keV
	66%	-	-	1654.9 keV	1616.3 keV
Panel2-1	70%	-	-	1690.9 keV	1651.7 keV
	80 %	-	-	1794.1 keV	1752.9 keV
	66%	-	-	1654.1 keV	1615.6 keV
Panel2-2	70%	-	-	1695.6 keV	1656.3 keV
	80 %	-	-	1799.5 keV	1758.2 keV
	66%	1634.9 keV	1656.7 keV	-	-
Panel1-1-30min	70%	1668.9 keV	1691.0 keV	-	-
	80 %	1766.9 keV	1789.9 keV	-	-
	66%	1743.6 keV	1768.1 keV	-	-
Panel2-1-30min	70%	1777.7 keV	1802.5 keV	-	-
	80 %	1874.4 keV	1900.5 keV	-	-

Table 7.12.: MIP Peak identification for all measurements with the MIP ADC values taken from either the measurements without source, with Cs137 or Co60. The highlighted values considering the 70% interpretation of the Compton edge represent the best valuated results.

8. Summary and outlook

The surface expansion of the IceCube Neutrino Observatory, the Surface Array Enhancement, is under development with a prototype station already in operation at the South Pole. The objective of this analysis is to verify the functionality of the scintillation detectors and characterise their energy response. This was done by performing an energy calibration of the detectors with radioactive sources, namely Na22, Cs137 and Co60. As the decay spectrum of these radioactive sources is well-studied and evolved, it can be utilised to set an energy reference for the digitized signal (the ADC channel) from the scintillators. While performing a measurement with a radioactive source nearby the scintillation detector, the Compton energy deposit can be observed in the charge spectrum recorded by the scintillators. Figure 8.1 shows the experimental setup with the scintillation panels and the utilized radioactive sources.

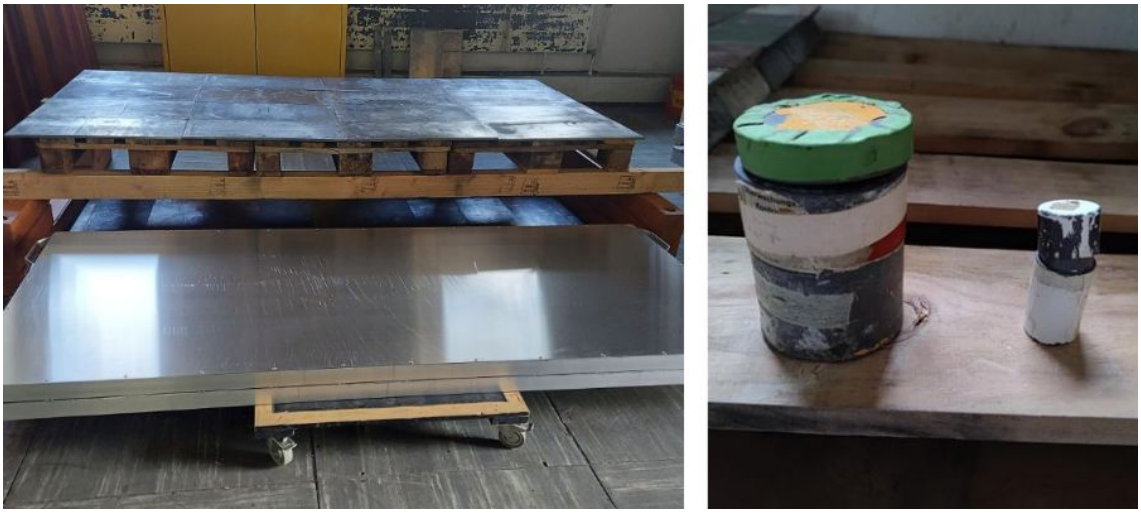

Figure 8.1.: The experimental setup for one of the measurement series. Left: The panel installation with a source placed on the surface of the detectors between the lead shielding. Right: The sources in their transportable shielding.

Prior to conducting the measurements, the experimental requirements were investigated, and the need for shielding from background radiation was confirmed. Moreover a varying positioning of the sources ascertained the uniformity of the scintillator panel itself. The influence of the threshold was examined and it was established, that a lower threshold increases the counts of the dark noise, compromising the measurements of the MIP peak. A threshold low enough to get a distinguished MIP peak, but simultaneously optimized against the recording of the dark count was found and utilised. The measurement series took place at two different temperatures, which has a strong impact on the gain of the SiPM

and hence the charge spectra in ADC values. The distinctions in the physical properties of the particles, which trigger a charge deposit in the scintillators and result in a distinct shape of the charge spectrum follow a various distributions. The characteristics caused by the sources are interpreted as their Compton edges, since the scintillation material cannot resolve the individual photopeaks, due to the lack of strong-bonded shell electrons. The Compton edges from the sources in the charge spectrum correspond to 70 % value of the Gaussian fits to the Compton edges peaks. Whereas the MIP peak is fit by a Landau function based on parameters estimated with a Gaussian pre-fit. For each measurement series, a linear regression of the ADC-channel-energy assigned values is build gaining a linear coherence of ADC channel and energy. For the measurements conducted with less shielding (data of 2022), the strong background contributes to a higher uncertainties in the fits and consequently deviation from the linear regression fits. Figure 8.2 shows all calculated results with the Compton edge correspondence of 70%, where one measurement consists of the pedestal for both sources, two Compton edges for Na22 and one Compton edge for Cs137 (data set 2022) respectively Co60 (data set 2023). The highlighted range around 1.5 – 2.0 MeV represents the assumption of the MIP peak energy range as well as the horizontal line the value gained from the Landau MIP peak fit and concludes a good alignment with the linear regression built from the ADC-channel-energy coherence.

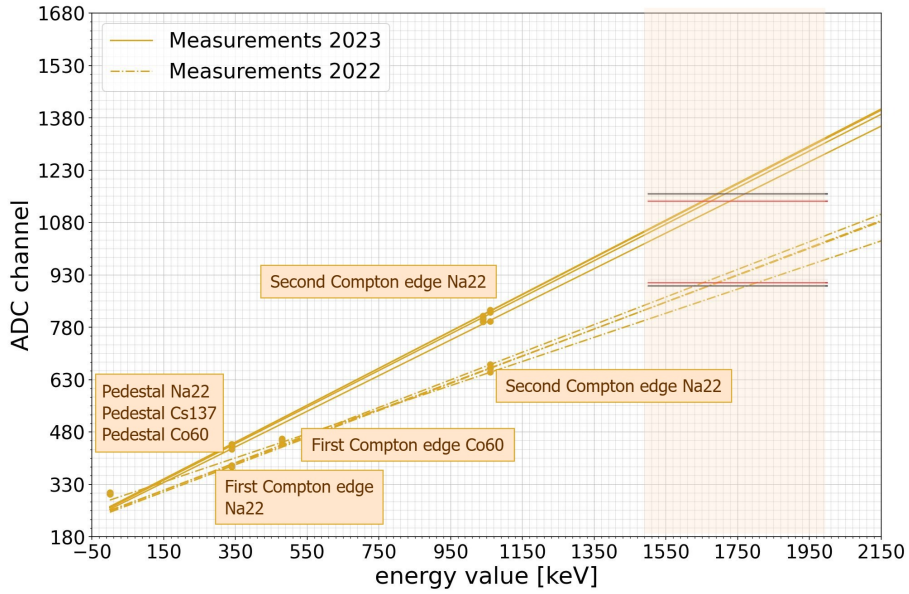

Figure 8.2.: Summary of the measurement results for both data sets (2022 and 2023). The black horizontal lines denote the weighted mean of the MIP peak measured by the measurements without source and the red ones are caused by the measurements with Cs137 (2022) respectively Co60 (2023).

Nevertheless, as already mentioned several uncertainties influence the measurements, which was recognized in the error analysis presented. The background appears to have the most significant impact on the quality of the Gaussian and Landau fits. Moreover, as displayed before, a difference of approximately 15-20°C acts considerably upon the measurement. Therefore the performed energy characterization is only an experimental

validation of the deposited energy from the MIPs. This can be further developed with more sources and measurements at negative temperatures to understand how the linear behavior gets modified at South Pole conditions. In this case an analysis on the temperature influence on the digitized signal, the ADC channel, is required. Additionally, the choice of sources at KIT was limited not only by the energy range of the MIP, but also because safety regulations prohibited the use of other sources at the experimental setup location. An increase of the sources amount and therefore an improvement of the measurements quantity will deliver a stronger validation of the linear coherence. Furthermore the uncertainty on the fit could be minimized and the averaging unneeded through a more exact cable analysis. Therefore measurements with a cable without bending could be performed as well as a deeper analysis of the periodic peaks, which are probable caused by the cable. The review on the Compton edges also displays a major uncertainty regarding their interpretation. In the end a most probably count-rate of 70 % was presumed, specific for plastic scintillators. But, as mentioned, it is a widely discussed scientific problem, which still leaves a margin for interpretation and is in need of a deeper understanding.
Nonetheless, the analysis and results of this detail of the entire energy calibration chain provides a validation of the main objective as well as a confirmation of the assumptions of the MIP peak position. The estimated linearity demonstrates the ADC-channel-energy coherence, opening opportunities for further research involving an expanded experimental setup and analysis. Therefore, the results provide valuable constraints for the analysis of the scintillator data utilizing comparison with Monte Carlo simulations of air-showers.

Bibliography

[1] Alessandro De Angelis. "Domenico Pacini, uncredited pioneer of the discovery of cosmic rays". In: *Rivista del Nuovo Cimento* (2011). URL: https://doi.org/10.1393/ncr/i2011-10060-9.

[2] Todor Stanev. *High Energy Cosmic Rays*. Third edtition. Cham: Springer International Publishing, 2021. ISBN: 978-3-030-71567-0.

[3] IceCube Collaboration. *Life at the Pole*. URL: https://icecube.wisc.edu/gallery/life-at-the-pole/. accessed: 28.01.2023 16:28.

[4] A. S. Leszczyńska. *Potential of the IceTop Enhancement with a Scintillation Detector Array*. Dissertation. Karlsruhe Institute of Technology, 2021. DOI: 10.5445/IR/1000131245.

[5] M. Oheler. *The Prototype Station for the IceCube Surface Array Enhancement*. Dissertation. Karlsruher Institute of Technology, 2021. DOI: 10.5445/IR/1000142813.

[6] Frank G. Schröder. "Radio detection of Cosmic-Ray Air Showers and High-Energy Neutrinos". In: *Progress in Particle and Nuclear Physics* 39 (2017), pp. 1–68. URL: https://doi.org/10.1016/j.ppnp.2016.12.002.

[7] Cern. *Cosmic rays: particles from outer space*. URL: https://home.cern/science/physics/cosmic-rays-particles-outer-space. accessed: 25.05.2023 14:30.

[8] Victor F. Hess. "Über Beobachtungen der durchdringenden Strahlung bei sieben Freiballonfahrten". In: *Phys. Z. 13* (1912), pp. 1084.

[9] Claus Grupen. *Neutrinos, Dark Matter and Co.: From the Discovery of Cosmic Radiation to the latest Results in Astroparticle Physics*. First edtition. Wiesbaden: Springer Fachmedien Wiesbaden, 2021. ISBN: 978-3-658-32547-3.

[10] Claus Grupen. *Astroparticle Physics*. Second edtition. Berlin: Springer Nature Switzerland, 2020. ISBN: 978-3-030-27339-2.

[11] Maurizio Spurio. *Probes of Multimessenger Astrophysics: Charged cosmic rays, neutrinos, gamma-rays and gravitational waves*. Second edtition. Cham: Springer International Publishing, 2018. ISBN: 978-3-319-96854-4.

[12] M. Tanabashi et al. (Particle Data Group). In: *Phys. Rev. D 98 030001* (2018). URL: https://doi.org/10.1103/PhysRevD.98.030001.

[13] Claus Grupen. *Astroteilchenphysik - Das Universum im Licht der kosmischen Strahlung*. First edtition. Braunschweig/Wiesbaden: Friedr. Vieweg Sohn Verlagsgesellschft mbH, 2000. ISBN: 3-528-03158-1.

[14] M. Oehler. *Characterization of SiPMs for the Surface Array Enhancement of IceCube*. Master Thesis. Karlsruhe Institute of Technology, 2021.

[15] H. Kolanoski et al. *Teilchendetektoren: Grundlagen und Anwendungen*. First edtition. Cham: Springer International Publishing, 2016. ISBN: 3-662-45349-5.

[16] H. Tokuno et. al. "New air fluorescence detectors employed in the Telescope Array experiment". In: *Nuclear Instruments and Methods in Physics Research A* 676 (2012). URL: https://doi.org/10.48550/arXiv.1201.0002.

[17] Thomas Huber. *IceScint: A Scintillation Detector Array for the IceCube Surface Enhancement*. Dissertation. Karlsruhe Institute of Technology, 2020. DOI: 10.5445/IR/1000131545.

[18] Magic Group. *The MAGIC Telescopes*. URL: https://magic.mpp.mpg.de/. accessed: 09.05.2023 22:45.

[19] R. Turcotte-Tardif. *Commissioning of the Radio Array for the IceCube Surface Enhancement focusing on High-Energy Cosmic Rays*. Dissertation. Karlsruhe Institute of Technology, 2022.

[20] Glenn F. Knoll. *Radiation Detection and Measurement*. First edtition. New York: John Wiley, 1979. ISBN: 0-471-49545-X.

[21] IceCube Collaboration: R. Abbasi et al. "IceTop: The surface component of IceCube". In: *arXiv e-prints* (2012). URL: https://doi.org/10.48550/arXiv.1207.6326.

[22] IceCube Collaboration: M. G. Aartsen et al. "The IceCube Neutrino Observatory: Instrumentation and Online Systems". In: *Jinst 12.03* P03012 (2017). URL: https://doi.org/10.48550/arXiv.1612.05093.

[23] IceCube Collaboration: M. G. Aartsen et al. "Cosmic ray spectrum and composition from PeV to EeV 3 years of data from IceTop and IceCube". In: *Phys. Rev. D 100.8* 082002 (2019). URL: https://doi.org/10.48550/arXiv.1906.04317.

[24] IceCube Collaboration. *Detector*. URL: https://icecube.wisc.edu/gallery/detector/. accessed: 28.01.2023 16:28.

[25] T. Benson et al. "IceCube Enhanced Hot Water Drill functional description". In: *Annals of Glaciology* (2014), 55(68). URL: https://doi.org/10.3189/2014AoG68A032.

[26] IceCube Collaboration. *Digital Optical Module Developement*. URL: https://icecube.wisc.edu/gallery/digital-optical-module-dom-development/. accessed: 28.01.2023 16:28.

[27] IceCube Collaboration. "IceCube - Detector". In: (2014). URL: https://icecube.wisc.edu/science/icecube/. accessed: 13.04.2023 08:16.

[28] IceCube Collaboration: Frank G. Schröder. "Science Case of a Scintillator and Radio Surface Array at IceCube". In: *PoS ICRC2019* (2020), p. 418. URL: https://doi.org/10.48550/arXiv.1908.11469.

[29] IceCube Collaboration: Andreas Haungs. "A Scintillator and Radio Enhancement of the IceCube Surface Detector Array". In: *EPJ Web of Conferences 210* 06009 (2019). URL: https://doi.org/10.1051/epjconf/201921006009.

[30] IceCube-Gen2 Collaboration: M. G. Aartsen et al. “IceCube-Gen2: The Window to the Extreme Universe”. In: *Journal of Phyics G: Nucleas and Particle Physics* 48.6 (2020). URL: https://doi.org/10.48550/arXiv.2008.04323.

[31] T. Karg et al. “Introducing TAXI: A Transportable Array fo eXtremely large area Instumentation studies”. In: *arXiv e-prints* (2014). URL: https://doi.org/10.48550/arXiv.1410.4685.

[32] IceCube Collaboration: S. Kunwar et al. “The IceTop Scintillator Upgrade”. In: *PoS* ICRC2017 (2018). DOI: 10.22323/1.301.0401.

[33] IceCube Collaboration: M. Oehler et al. “Development of a scintillation and radio hybrid detector array at the South Pole”. In: *PoS* ICRC2021 (2021). URL: https://doi.org/10.48550/arXiv.2107.09983.

[34] D. Beznolsko et al. “FNAL-NICADD extruded scintillator”. In: *Nuclear Science Symposium Conference Record* 2 (2004). DOI: 10.1109/NSSMIC.2004.1462328.

[35] P. Sigmund. *General aspects and stopping of swift point charges*. First edtition. Berlin: Springer, 2006. ISBN: 3-540-31713-9.

[36] Kuraray: Plastic Scintillating Fibers. *Wavelength Shifting Fibers*. URL: http://kuraraypsf.jp/psf/ws.html. accessed: 28.01.2023 16:28.

[37] IceCube Collaboration: Thomas Huber et al. “The IceTop Scintillator Upgrade”. In: *PoS* ICRC2017 (2018). URL: https://doi.org/10.22323/1.301.0401.

[38] *Private communication with Thomas Huber*. 2023.

[39] Hamatsu Photonics Deutschland. *MPPC S13360 series*. URL: https://www.hamamatsu.com/resources/pdf/ssd/s13360_series_kapd1052e.pdf. accessed: 28.01.2023 16:28.

[40] IceCube Collaboration: M. Kauer et al. “The Scintillator Upgrade of IceTop:Performance of the prototype array”. In: *PoS* ICRC2019 (2019). URL: https://doi.org/10.48550/arXiv.1908.09860.

[41] X. Li et al. “Energy calibration for plastic scintillation detectors based on Compton scatterings of gamma rays”. In: *JINST* 12 (2017), P12025. URL: https://iopscience.iop.org/article/10.1088/1748-0221/12/12/P12025/pdf.

[42] Christian Plonka. *Verbesseerung dere Lichtauskopplung zur Messung der Neutrinoasymmetrie mit PERKEO II*. Diplomarbeit, Ruprecht-Karls-Universität Heidelberg, 2000. URL: https://www.physi.uni-heidelberg.de/Publications/dipl_plonka.pdf.

[43] *Private communication with Joachim Wolf*. 2023.

[44] Particle Data Group. *27. Passage of particles through matter*. 2005. URL: https://pdg.lbl.gov/2005/reviews/passagerpp.pdf. Access date: 11.05.2023, 14:53.

[45] H. Daniel. “Die Formen der ß-Spektren von Na^{22}, Na^{24} und P^{23}”. In: *Nuclear Physics* 8 (1958), pp. 191–198. URL: https://doi.org/10.1016/0029-5582(58)90147-0.

[46] Hyun Cheol Lee et al. "Validation of energy-weighted algorithm for radiation portal monitor using plastic scintillator". In: *Applied Radiation and Isotopes* (2016). DOI: 10.1016/j.apradiso.2015.10.019.

[47] E. Auffray et. al. "Characterization studies of Silicon Photomultipliers and crystals matrices for a novel time of flight PET detector". In: *Journal of Instrumentation* 10 (2015). DOI: 10.1088/1748-0221/10/06/P06009.

[48] M. Ashraf et al. "Cesium-137: Radio-Chemistry, Fate, and Transport, Remediation, and Future Concerns". In: *Critical Reviews in Environmental Science and Technology* (2014). DOI: 10.1080/10643389.2013.790753.

[49] E. Andreotti et al. "^{130}Te neutrinoless double-beta decay with CUORICINO". In: *Astroparticle Physics* 34 (2011), pp. 822–831. URL: https://doi.org/10.1016/j.astropartphys.2011.02.002.

[50] M. Tohamy. "Reevaluation of the neutron emission probabilities from 241Am–Be neutron source". In: *Nuclear instruments and methods in physics research section A* 942 (2019). URL: https://doi.org/10.1016/j.nima.2019.162387.

[51] P. Pasuthip. *Characterization of Pulse.Shape Discrimination for Background Reduction in the DEAP-1 Detector*. Master Thesis, Queen's University, 2009. URL: https://qspace.library.queensu.ca/bitstream/handle/1974/1688/Pasuthip_Paradorn_200901_MSc.pdf.

[52] M. J. Safari et al. "Differentiation method for localization of Compton edge in organic scintillation detectors". In: *Instrumentation and Detectors* (2016). URL: https://doi.org/10.48550/arXiv.1610.09185.

[53] L. Beghian et al. "A fast neutron spectrometer capable of nanosecond time gating". In: *Nuclear Instruments and Methods* 35 (1965), pp. 34–44. URL: https://doi.org/10.1016/0029-554X(65)90004-2.

[54] H. Knox et al. "A technique for determining bias settings for organic scintillators". In: *Nuclear Instruments and Methods* 101 (1972), pp. 519–525. URL: https://doi.org/10.1016/0029-554X(72)90040-7.

[55] R. Honecker et al. "Detection efficiency of plastic scintillator for neutrons between 0.2 and 3 MeV". In: *Nuclear Instruments and Methods* 46 (1967), pp. 282–288. URL: https://doi.org/10.1016/0029-554X(67)90084-5.

[56] M. J. M. Duke et al. "A precise method to determine the activity of a weak neutron source using a germanium detector". In: (2016). URL: http://dx.doi.org/10.1016/j.apradiso.2016.06.032.

[57] H. Lee et al. "Validation of energy-weighted algorithm for radiation portal monitor using plastic scintillator". In: *Applied Radiation and Isotopes: Including Data, Instrumentation and Methods for Use in Agriculture, Industry and Medicine* 107 (2016), pp. 160–164. URL: DOI:10.1016/j.apradiso.2015.10.019.

A. Appendix

A.1. Cable tests

Figure A.1 displays the estimated MIP position fit by a Landau distribution.

A.2. Threshold choice

Figure A.1 shows the measurement without a source with varying threshold, recorded by panel 1.

A.3. Experimental setup

Figure A.2 shows a closer look on the experimental setup and figure A.3 the two sources Na22 and Cs137.

A.4. Fit results

A.4.1. Without source

Data set 2022

Figure A.4 displays the fit measurements by panel 1 and A.5 by panel 2 of the data set from 2022.

Data set 2023

Figure A.6 collects the fit results for the measurements without source in 2023 by panel 1 and A.7 by panel 2.

A.4.2. Sodium22

Data set 2022

Figure A.8 collects the fit results for the measurements with Na22 in 2022.

Data set 2023

Figure A.9 collects the fit results for the measurements with Na22 in 2023.

Cable number	Fitted MIP position
19	960.339
20	957.241
21	957.972
22	960.261
24	962.421
25	968.755
26	957.196
27	960.307
28	957.470
31	962.456
32	958.203
36	961.376
37	958.144
38	954.157
39	959.117
40	960.202
41	956.687
42	954.222
43	961.295
44	959.210
45	959.407
46	956.854

Table A.1.: Fitting results for the MIP of the cable measurement.

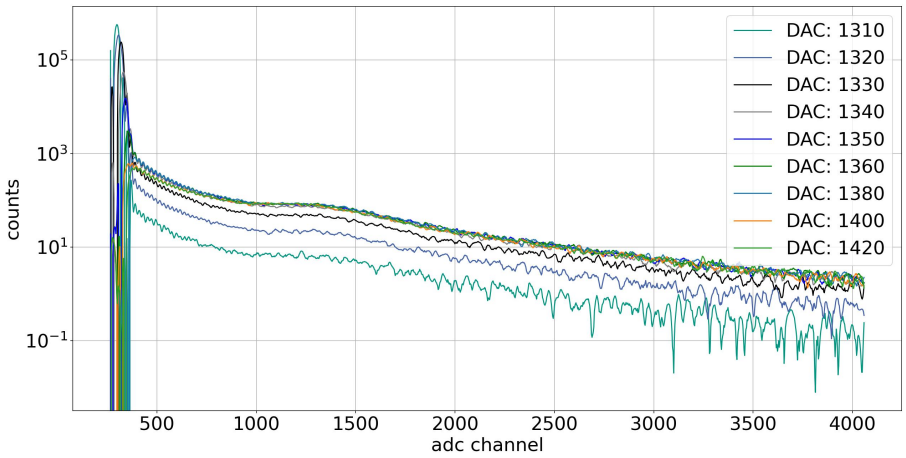

Figure A.1.: Charge histograms for the different threshold measured by panel 1, without source for a duration of 5 minutes.

Figure A.2.: A closer look of the experimental setup of the measurements 2023 with a source placed in between the panels.

Figure A.3.: Pictures of the two sources Na22 and Cs137.

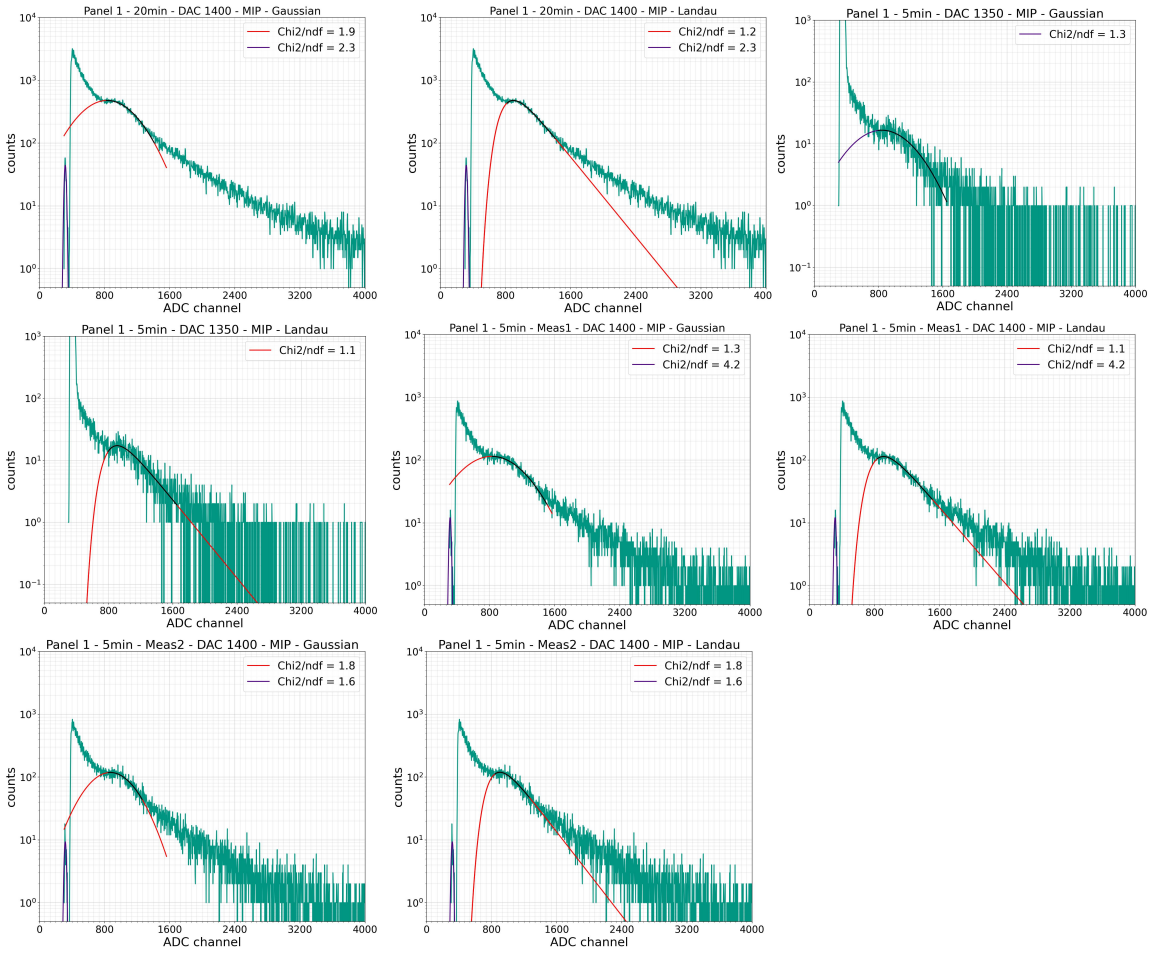

Figure A.4.: Without source - panel 1 - 2022

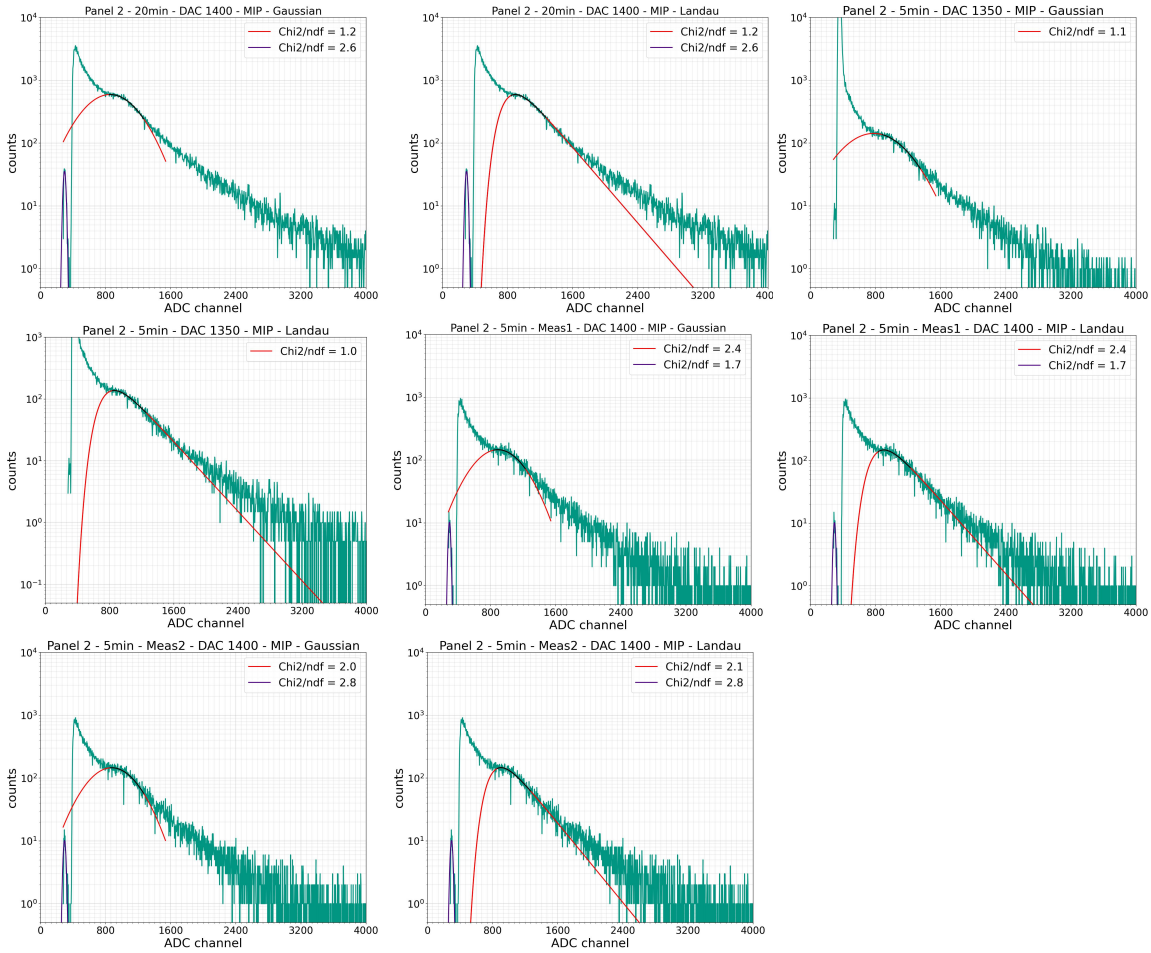

Figure A.5.: Without source - panel 2 - 2022

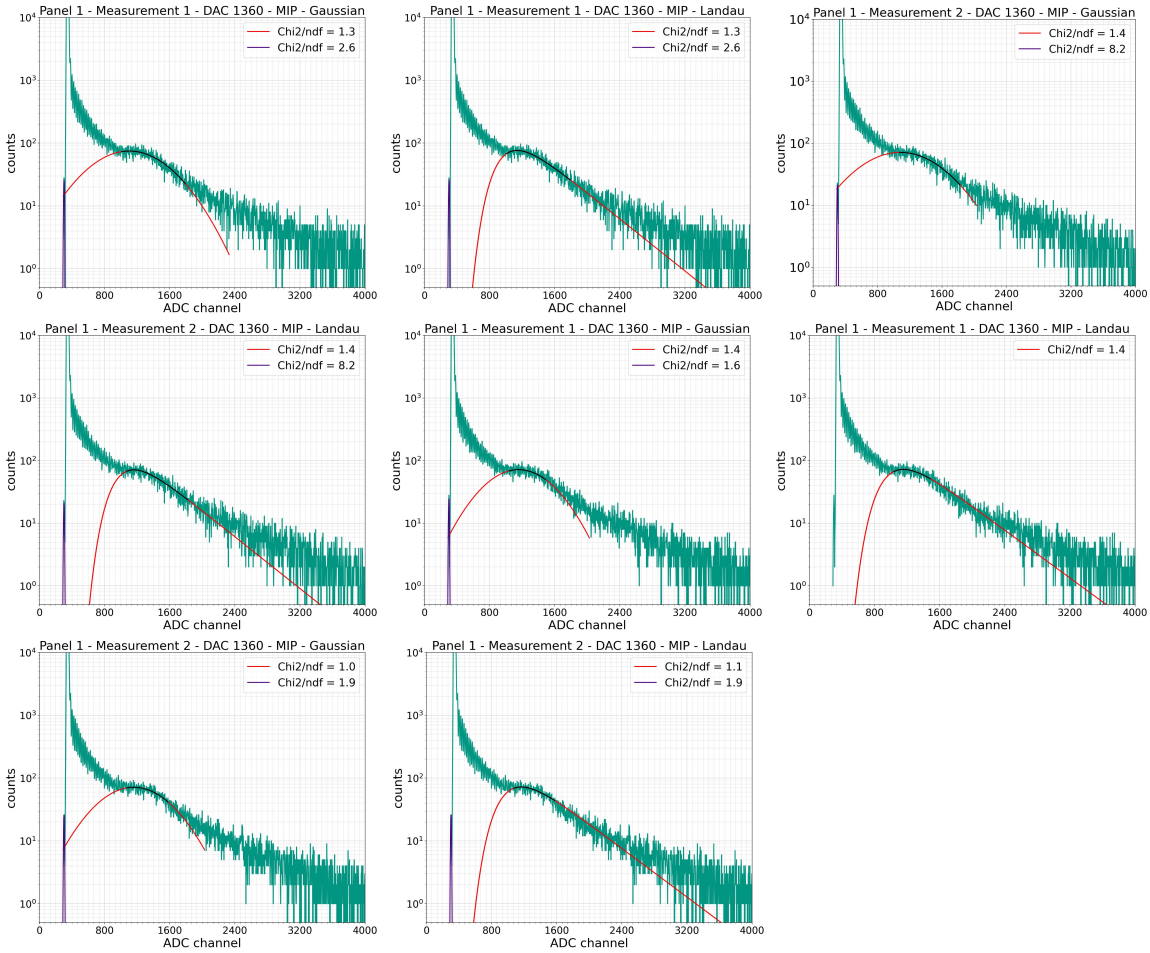

Figure A.6.: Without source - panel 1 - 2023

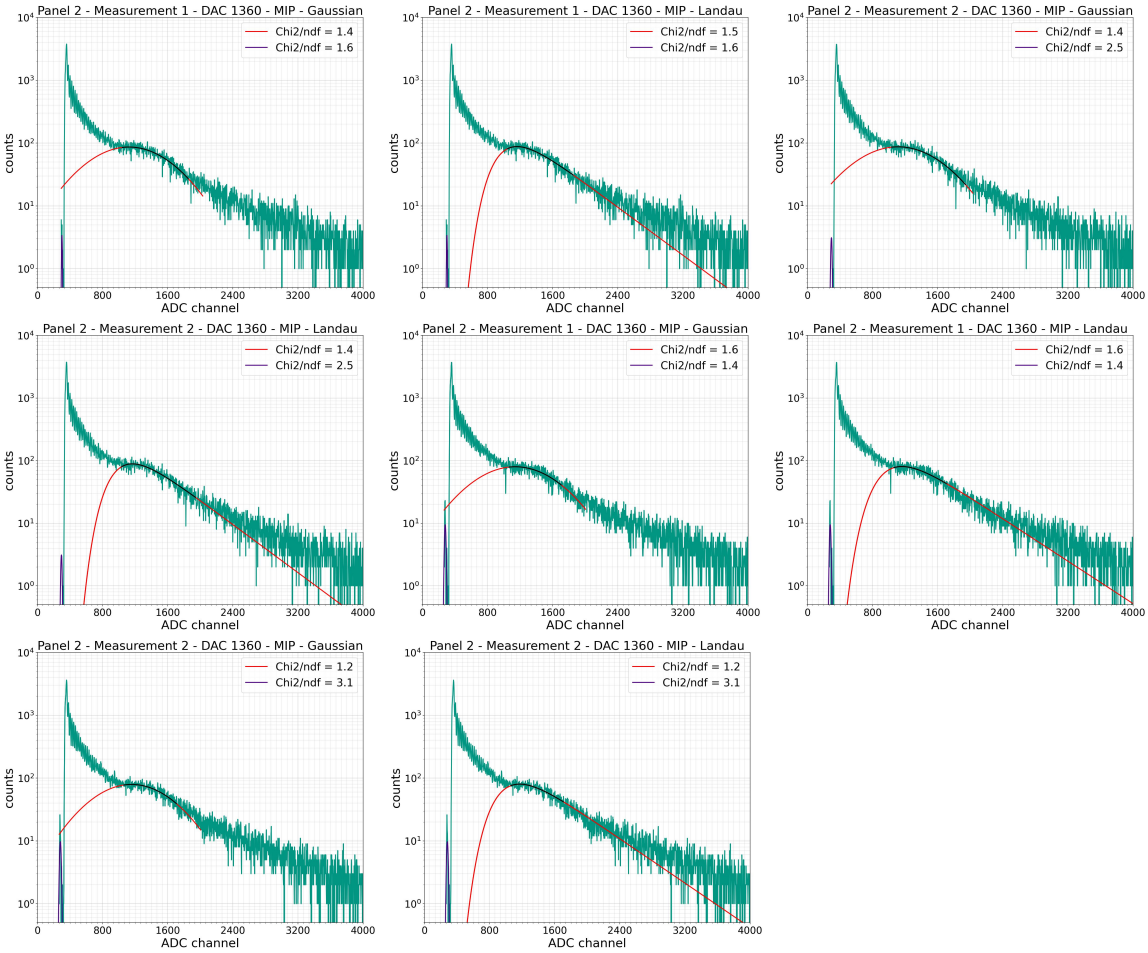

Figure A.7.: Without source - panel 2 - 2023

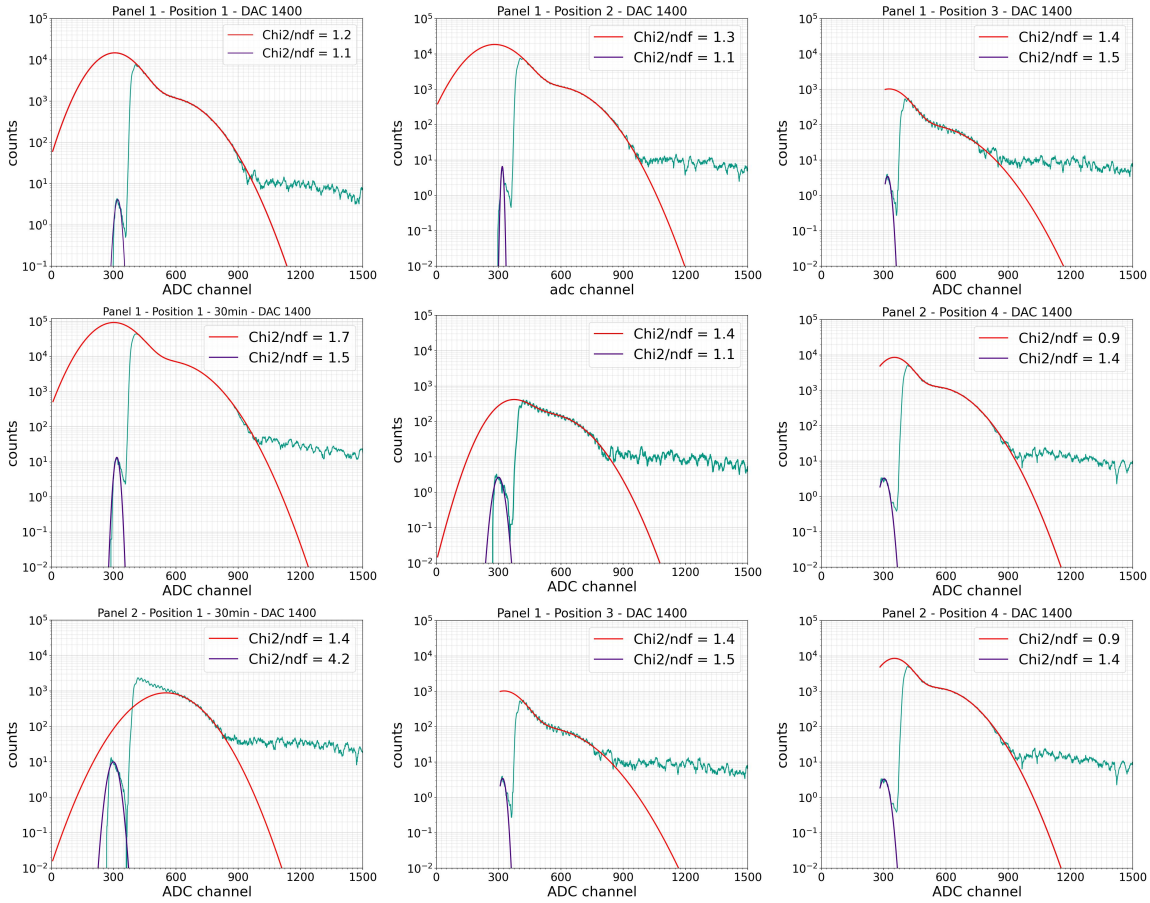

Figure A.8.: Na22 - 2022

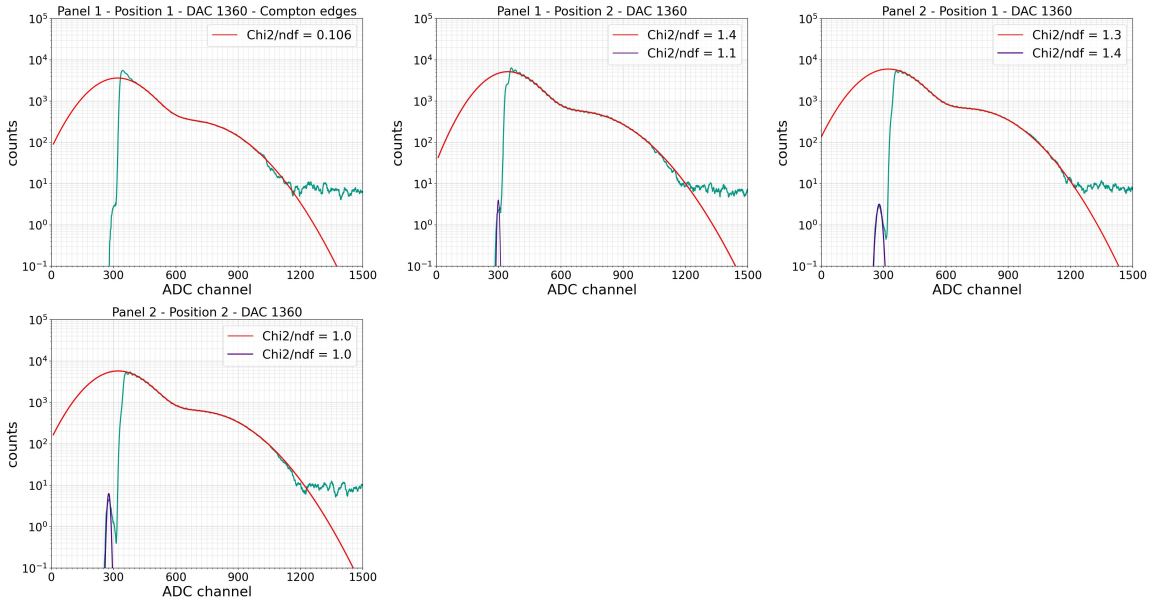

Figure A.9.: Na22 - 2023

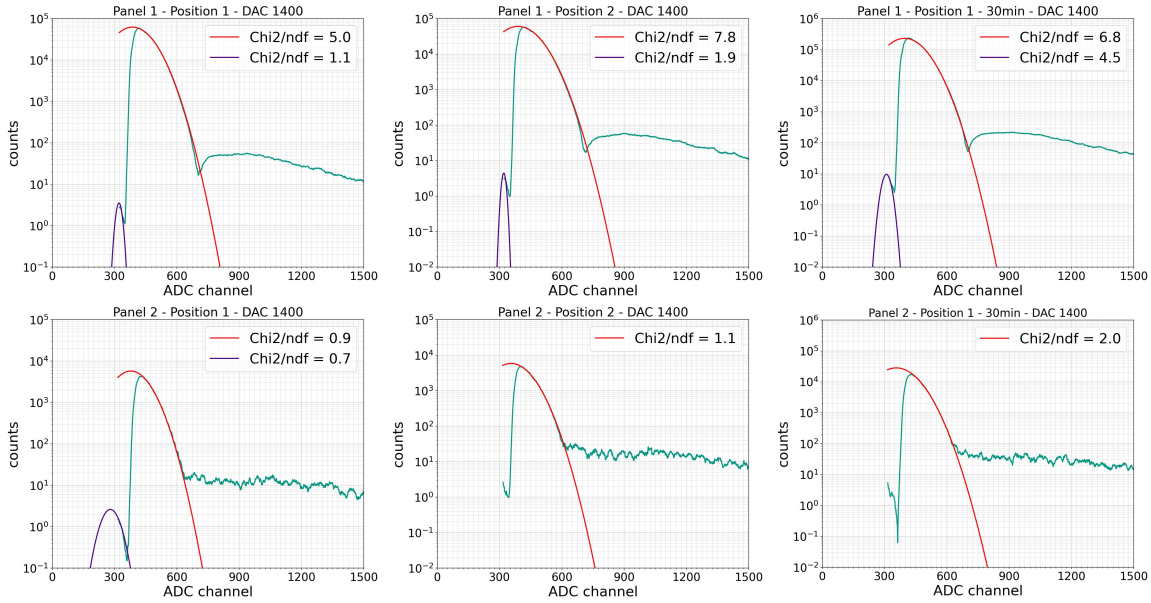

Figure A.10.: Cs137 - 2022 - Compton edges

Measurement	Slope	Chi-squared test
Panel 1 - 5 min - Position 1	$ADC_{value} = (0.38 \pm 0.01) * E_x + (255.3 \pm 8.7)$	$\frac{Chi^2}{ndf} = 5.5$
Panel 1 - 5 min - Position 2	$ADC_{value} = (0.40 \pm 0.01) * E_x + (250.9 \pm 8.6)$	$\frac{Chi^2}{ndf} = 6.5$
Panel 1 - 30min - Position 1	$ADC_{value} = (0.39 \pm 0.02) * E_x + (252.5 \pm 12.7)$	$\frac{Chi^2}{ndf} = 9.6$
Panel 2 - 30min Position 1	$ADC_{value} = (0.35 \pm 0.01) * E_x + (284.7 \pm 14.1)$	$\frac{Chi^2}{ndf} = 1.7$

Table A.2.: ADC-energy relation for the measurements of 2022.

A.4.3. Cesium137

Figure A.10 collects the fit results of the Compton edges for the measurements with Cs137 in 2022 and A.11 the results of the MIP fits.

Cobalt60

Figure A.12 collects the fit results of the Compton edges for the measurements with Co60 in 2023 and A.13 the results of the MIP fits.

A.5. Linear coherence

A.5.1. Linear regression - 2022

Figure 7.10 collects the linear regressions of all calculations with the 2022 data set.

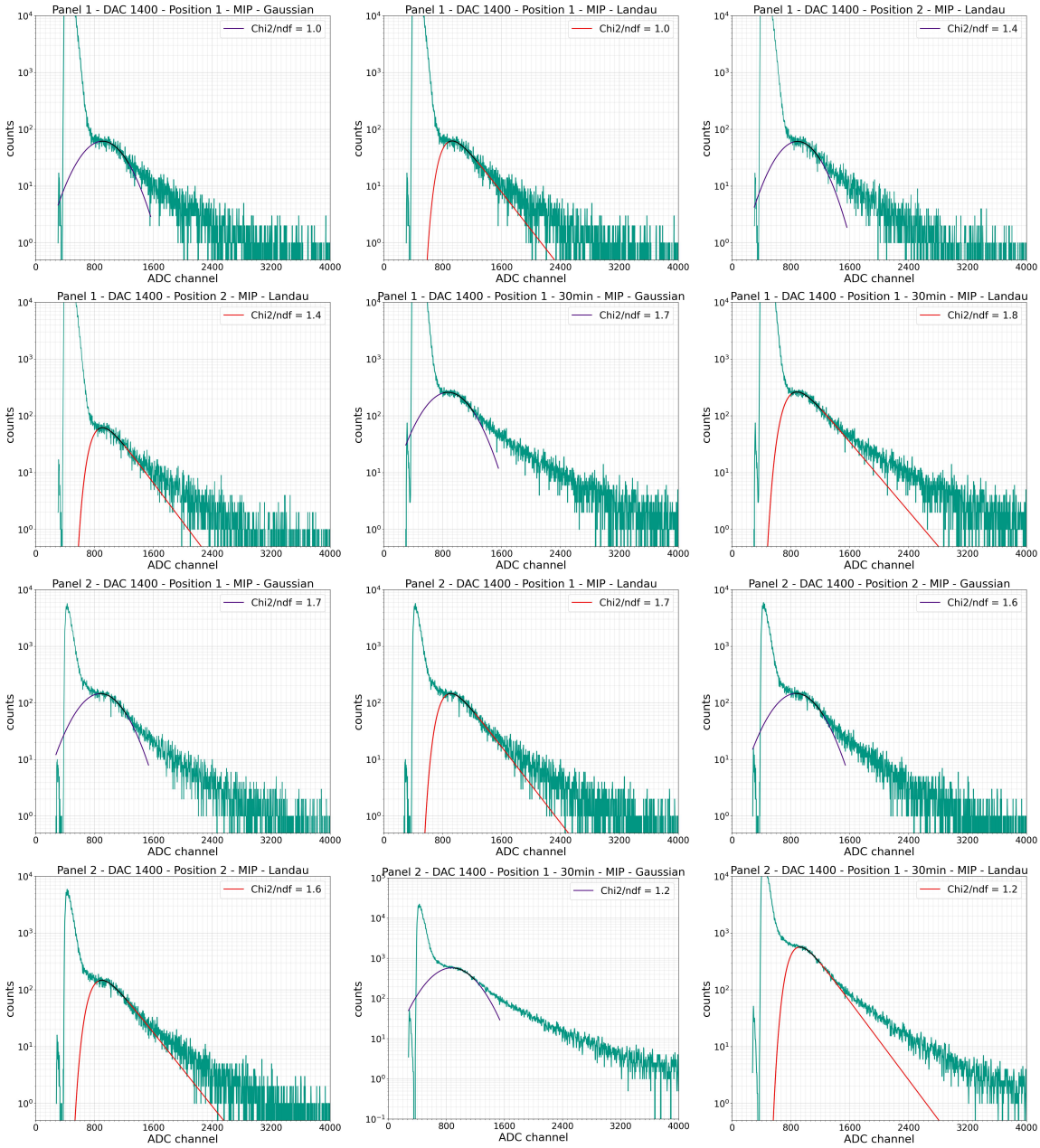

Figure A.11.: Cs137 - 2022 - MIP

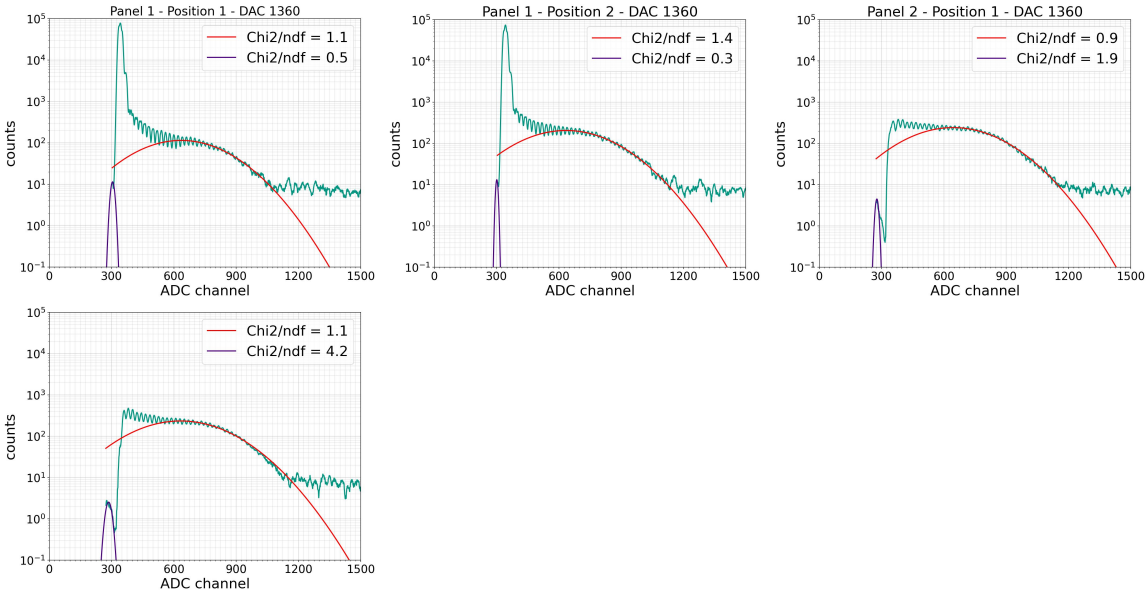

Figure A.12.: Co60 - 2023 - Compton edges

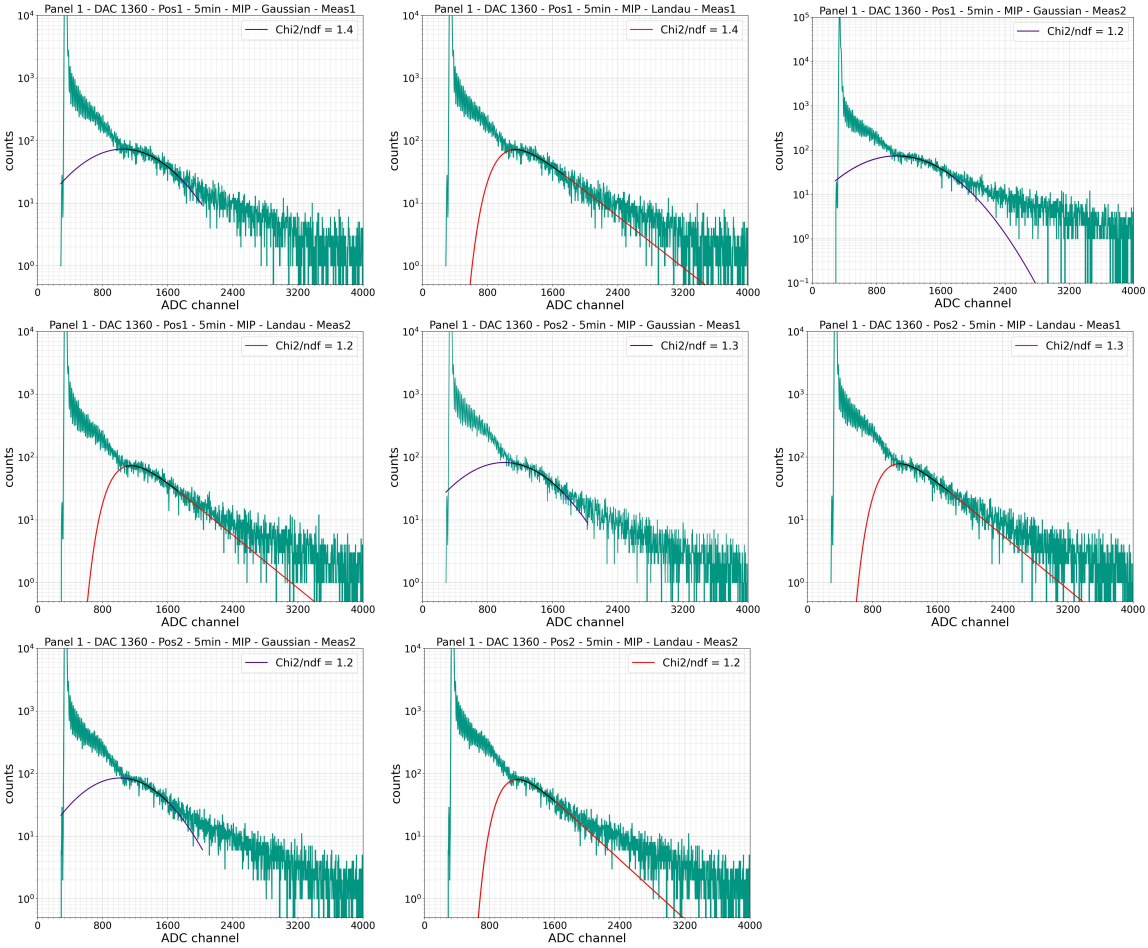

Figure A.13.: Cobalt -2023 - MIP

Measurement	Slope	Chi-squared test
Panel 1 - 5 min - Position 1	$ADC_{value} = (0.51 \pm 0.01) * E_x + (258.1 \pm 8.9)$	$\frac{Chi^2}{ndf} = 3.7$
Panel 1 - 5 min - Position 2	$ADC_{value} = (0.52 \pm 0.01) * E_x + (262.8 \pm 10.7)$	$\frac{Chi^2}{ndf} = 3.0$
Panel 2 - 5 min - Position 1	$ADC_{value} = (0.53 \pm 0.01) * E_x + (264.5 \pm 10.3)$	$\frac{Chi^2}{ndf} = 2.7$
Panel 2 - 5 min - Position 2	$ADC_{value} = (0.53 \pm 0.01) * E_x + (265.9 \pm 9.9)$	$\frac{Chi^2}{ndf} = 2.5$

Table A.3.: ADC-energy relation for the measurements of 2023.

A.5.2. Linear regression - 2023

Figure 7.11 collects the linear regressions of all calculations with the 2023 data set.

Acknowledgments

This thesis would not have been possible without many friendly and helpful people. I want to express my thanks to...

... Prof. Ralph Engel for beeing the referee of this thesis and the oppertunity to write my bachelor thesis at the IAP.

... Dr. Andreas Haungs for always supporting and supervising me in a motivating and humorous way.

... Shefali for her open ear, her advises and her great input at any time of the day.

... Thomas Huber, who introduced me into IceCube and had always good advises and deeper knowledge.

...Donghwa Kang and Dennis Soldin, who made my start at the IceCube group very pleasant.

... Federico Bontempo, who always had a helping hand when needed.

... Joachim Wolf for providing me with the radioactive sources as well as information about their characteristics.

... Thomas Lobmaier for saving me, when i got stuck in the python code.

... the whole IceCube and CRT group at KIT.